ChemComm

ROYAL SOCIETY OF CHEMISTRY

FEATURE ARTICLE

View Article Online
View Journal | View Issue

Cite this: *Chem. Commun.*, 2025, **61**, 15145

Layered double hydroxides in catalyzing the green hydrogen revolution: advancements and prospects

Priyadarshi Roy Chowdhury, [a] Himani Medhi, [b] Krishna G. Bhattacharyya [c] and Chaudhery Mustansar Hussain *[d]

Layered double hydroxides (LDHs) are emerging as critical materials for advancing the green hydrogen economy due to their versatility, cost-effectiveness, and tunable catalytic properties. Their layered structure allows for compositional flexibility, enabling optimization of active sites for efficient electron transfer. The objective of this review is to comprehend the latest advancements in the production of sustainable LDHs with a particular emphasis on their potential for the efficient electrochemical water splitting process involving both seawater and freshwater, which is essential for the generation of green hydrogen as a sustainable energy source. The strategies of green hydrogen generation and its mechanism have been critically discussed in this review. An overview is provided on the concept of green hydrogen economy involving LDH-based materials. Ongoing research into the design and application of LDHs is anticipated to provide a sustainable avenue for green hydrogen by integrating high catalytic efficiency, resource optimisation, and adaptability to practical conditions such as seawater electrolysis, thus realising their complete potential in decarbonising energy systems.

Received 2nd June 2025,
Accepted 8th September 2025

DOI: 10.1039/d5cc03111g

rsc.li/chemcomm

1. Introduction

The need for the development of clean and sustainable energy is driven by several critical factors, including environmental protection, energy security, economic benefits, and global sustainability goals. Clean energy sources like solar, wind, green hydrogen and hydroelectric power significantly reduce greenhouse gas emissions, which are major contributors to climate change.[1] Renewable energy minimizes air pollution and water contamination, improving public health by reducing respiratory diseases and other health issues associated with fossil fuel emissions.[2] Renewable energy is crucial for meeting this goal and supporting sustainable development globally.[3] Sustainable energy ensures that current energy needs are met without compromising the ability of future generations to meet their own needs, aligning with the principle of intergenerational equity. Thus, the development of clean and sustainable energy is vital for addressing climate change, ensuring energy security, promoting economic growth, and achieving global sustainability goals.

The concept of a green hydrogen economy revolves around the use of hydrogen as a clean energy carrier, produced primarily through the electrolysis of water using renewable energy sources. This approach aims to significantly reduce greenhouse gas emissions and dependence on fossil fuels, contributing to a more sustainable energy system. Green hydrogen is produced by electrolyzing water using electricity generated from renewable sources like solar, wind, or hydroelectric power.[4] This process emits only water vapour and oxygen, making it a carbon-neutral energy source.[5] The development of a green hydrogen economy offers a promising pathway to decarbonize hard-to-abate sectors, enhance energy security, and support sustainable development goals.

Layered double hydroxides (LDHs) are emerging as pivotal materials in advancing the green hydrogen economy due to their structural versatility, cost-effectiveness, and catalytic efficiency. Hydrotalcite, the naturally occurring prototype of LDH, was first identified in 1842. A hundred years later, in 1942, researchers succeeded in synthesizing the first LDHs, which also led to the establishment of the double-layer sheet concept in their preparation. LDHs have evolved from a mineral curiosity to a cornerstone of sustainable technology, with ongoing research focused on scalability, durability, and multifunctional applications in energy and environmental systems. Fig. 1 displays the timeline associated with the development of LDH

[a] *Department of Chemistry, Gauhati University, Guwahati-781014, Assam, India. E-mail: priyadarshiroychowdhury@outlook.com*
[b] *Department of Chemistry, Eastern Karbi Anglong College, Sarihajan-782480, Assam, India. E-mail: himanimedhi18@gmail.com*
[c] *Department of Chemistry, Assam Don Bosco University, Sonapur-782402, Assam, India. E-mail: kgbhattacharyya@gmail.com*
[d] *Department of Chemistry and Environmental Science, New Jersey Institute of Technology, Newark, NJ 07102, USA. E-mail: chaudhery.m.hussain@njit.edu*

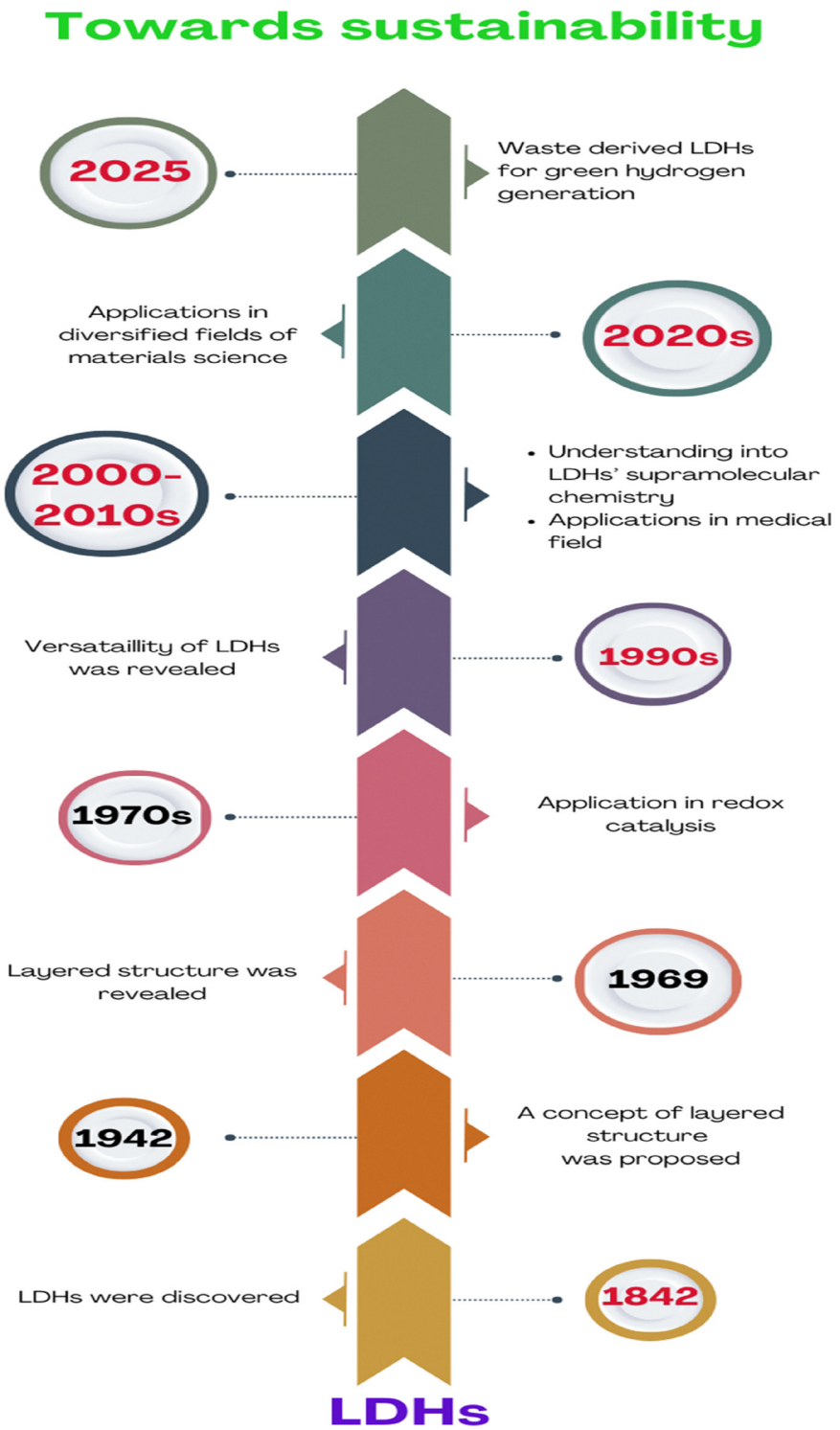

Fig. 1 Timeline associated with the development of LDH materials.

materials. Its layered structure and tunable composition enhance active site exposure and electron transfer. Defects and vacancies in LDHs, such as those created by dissolving M^{n+} ions, further could boost catalytic performance.[6] LDHs and their derivatives (*e.g.*, transition metal dichalcogenide composites) efficiently drive both oxygen evolution reaction (OER) and hydrogen evolution reaction (HER), enabling scalable electrolysis systems.[7] LDHs derived from industrial waste also align with circular economy principles.[8–10] The importance of this topic could be understood through the number of publications in ScienceDirect from 2021 to 2025 under the keyword 'layered double hydroxides for green hydrogen generation', depicted

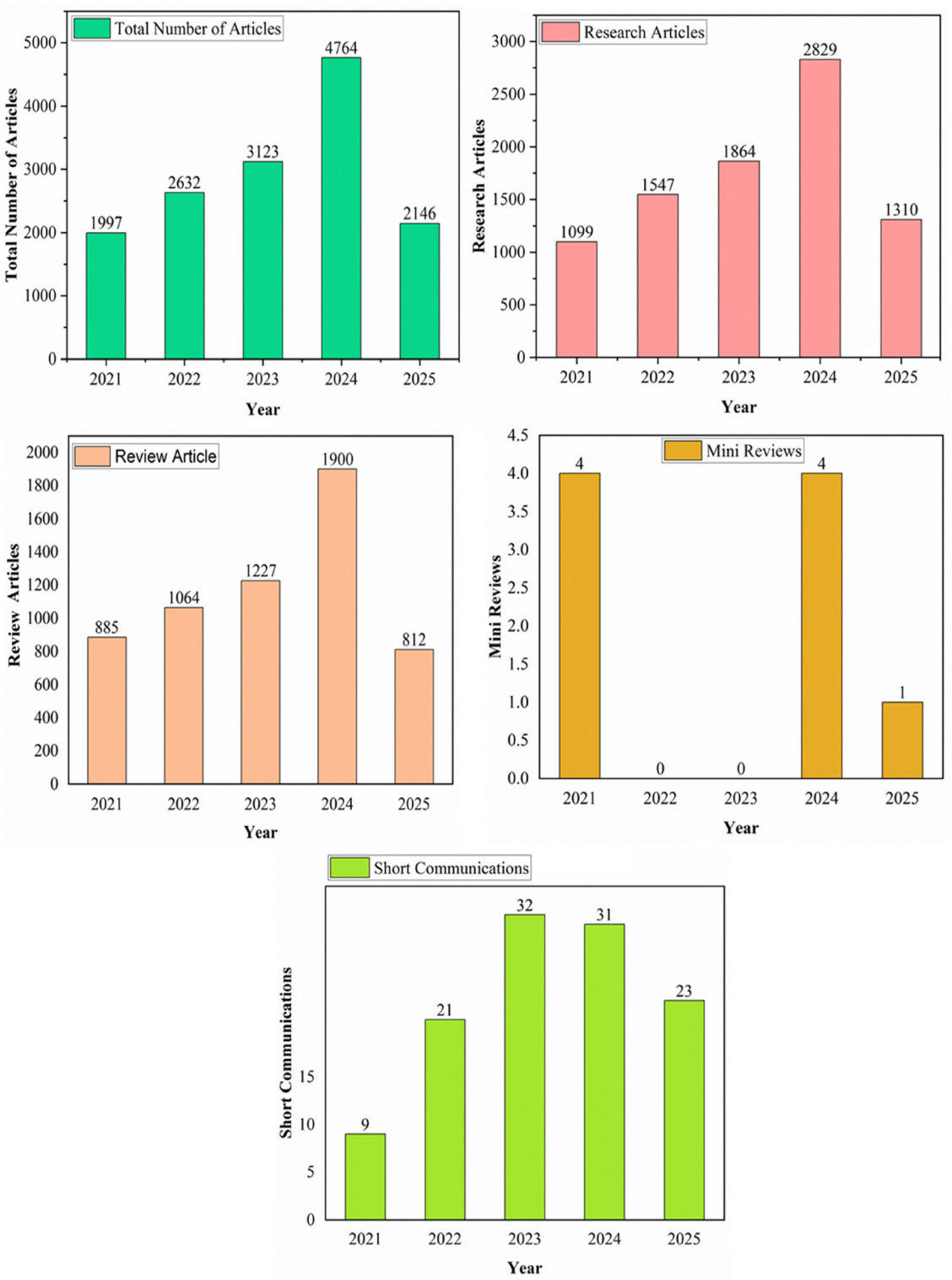

Fig. 2 The number of articles available in ScienceDirect under the keyword 'layered double hydroxides for green hydrogen generation' from 2021–2025 (accessed on 17/03/2025; 00:52 IST).

graphically in Fig. 2. LDHs could most likely address the challenges in seawater-based hydrogen production, since the hierarchical structures (*e.g.*, hollow microspheres) of LDH-based materials have been reported to improve the surface area and stability, critical for industrial-scale brine electrolysis.[8] Thus, LDHs bridge critical gaps in the green hydrogen value chain, from efficient water splitting to sustainable material sourcing, making them indispensable for achieving a

carbon-neutral energy future. Innovations in their design and application would likely continue to drive down costs and improve performance, accelerating the transition to clean energy systems.[11–23]

The objective of this review is to highlight the recent breakthroughs in LDH-based materials for sustainable hydrogen production, emphasizing their structural adaptability and versatility. The synthesis as well as functionalization strategies have also been mentioned in detail. The mechanistic pathways of these materials for HER, OER and overall water splitting (OWS) have been also been discussed in detail. Further, the review also emphasizes sustainable material design and waste utilization through the integration of a circular economy. It is anticipated that this review would bridge fundamental research and industrial applications by showcasing LDHs as versatile, scalable catalysts for green hydrogen production. Furthermore, this review also emphasizes the role of LDHs in reducing carbon footprints, enhancing energy efficiency, and aligning with global sustainability goals.

2. Strategies for green hydrogen generation with LDHs

LDHs have emerged as promising materials for green hydrogen production due to their tunable structure, high surface area, and catalytic properties. Recent advances in synthesis strategies focus on optimizing crystallinity, morphology, and sustainability while enhancing their performance in HER and OER. In this review, the compounds have been labelled following the notation used in the original research articles cited to maintain consistency with the primary sources and to avoid any disambiguity in material representation. The emerging strategies of LDH synthesis for green hydrogen generation are enlisted herein.

2.1. Hydrothermal synthesis

Hydrothermal synthesis has emerged as a key method for producing LDHs with optimized properties for green hydrogen generation. This approach enables precise control over crystallite size, morphology, and interlayer structure, directly impacting their performance in water splitting. Hydrothermal synthesis is generally dependent on the precursor. Both urea and hexamethylenetetramine (HMT) act as *in situ* ammonium-releasing agents, generating hydroxide ions under hydrothermal conditions, which are essential for the nucleation and growth of LDH layers, facilitating uniform LDH crystallization. Urea is more commonly used because it simultaneously supplies carbonate (a stabilizing interlayer anion) and OH^-, leading to phase-pure LDHs. On the other hand, HMT is often preferred when carbonate-free LDHs are required (*e.g.*, to study interlayer anion-exchange more easily). The choice between urea and HMT largely depends on the desired interlayer anion, reaction kinetics, and structural requirements of the target LDH. A study revealed that for ZnCr-LDHs and NiCr-LDHs, optimal results occur at 150 °C for ZnCr-LDH (88 μmol h^{-1} g^{-1} hydrogen generation rate at 50% methanol) and 200 °C for NiCr-LDH (41 μmol h^{-1} g^{-1}).[1] Moreover, time and heating rate significantly influence crystallization under hydrothermal processes. Slow heating (25 °C h^{-1}) with continuous stirring has been reported to enhance crystallinity. Extended durations (>1 day) have been reported to result in risk decomposition of ZnCr-LDH into $ZnCr_2O_4/Cr_2O_3$ phases.[14]

Table 1 Table illustrating the comparative performance of hydrogen generation using hydrothermally synthesised LDHs and LDH-based composites

Hydrothermal synthesis conditions	LDH type	Hydrogen output	Ref.
150 °C, HMT-mediated	ZnCr-LDH	88 μmol h^{-1} g^{-1}	14
200 °C, optimized crystallites	NiCr-LDH	41 μmol h^{-1} g^{-1}	14
Composite hydrothermal	Co–Al/GQD	8643 μmol g^{-1}	21

The hydrothermal process also results in crystallite size optimization. For ZnCr-LDH, the catalytic activity was found to increase steadily with crystallite size (up to about 18 nm), which was attributed to enhanced charge-carrier separation.[14] The hydrothermal synthesis process also has been reported to engineer morphologically the LDH structures. A separate study reported that Ni/Al-LDH nanorods synthesized at 180 °C exhibit enhanced surface area and stability, ideal for sustained catalytic activity.[3] Hydrothermal synthesis also follows green synthesis considerations involving waste utilization.[23] Hydrothermal methods have been reported to incorporate industrial byproducts while maintaining low energy inputs (*e.g.*, hydrocalumite synthesis from Ca/Al-rich waste). Hydrothermal processes also follow reduced chemical footprint (*e.g.*, HMT as a single precipitant) and align with sustainable production goals.[14,22] The comparative results of hydrogen production with some hydrothermally synthesized LDHs and LDH-based composites have been presented in Table 1. The schematic illustration of the different stages of hydrothermal synthesis of LDHs from waste precursors, involving the various stages of its formation, *viz.*, nucleation, growth, crystallization and aggregation leading to electrochemical water splitting, thereby generating green hydrogen and oxygen is presented in Fig. 3. The recent advancements highlight hydrothermal synthesis as a versatile route for tailoring LDH properties, with ongoing research focusing on scaling production and integrating machine learning for parameter optimization.

2.2. Green synthesis of LDHs

Green synthesis LDHs have emerged as a sustainable pathway for efficient hydrogen production, addressing environmental concerns and industrial scalability. These methods eliminate toxic solvents, reduce energy consumption, and enhance catalytic performance in water-splitting applications. The green solvent-free approach bypasses the traditional aqueous methods of LDH syntheses.[8] The green preparation technique improved synthesis efficiency, streamlined synthetic processes, and conserved water and raw resources, resulting in LDHs having rich interchangeable sites with enhanced sorption capabilities in an ultrathin framework. A recent study reported a solvent-free technique for the synthesis of a highly effective NiFe-LDH electrocatalyst for highly efficient OER and HER processes,[26] which has been schematically depicted in Fig. 4.

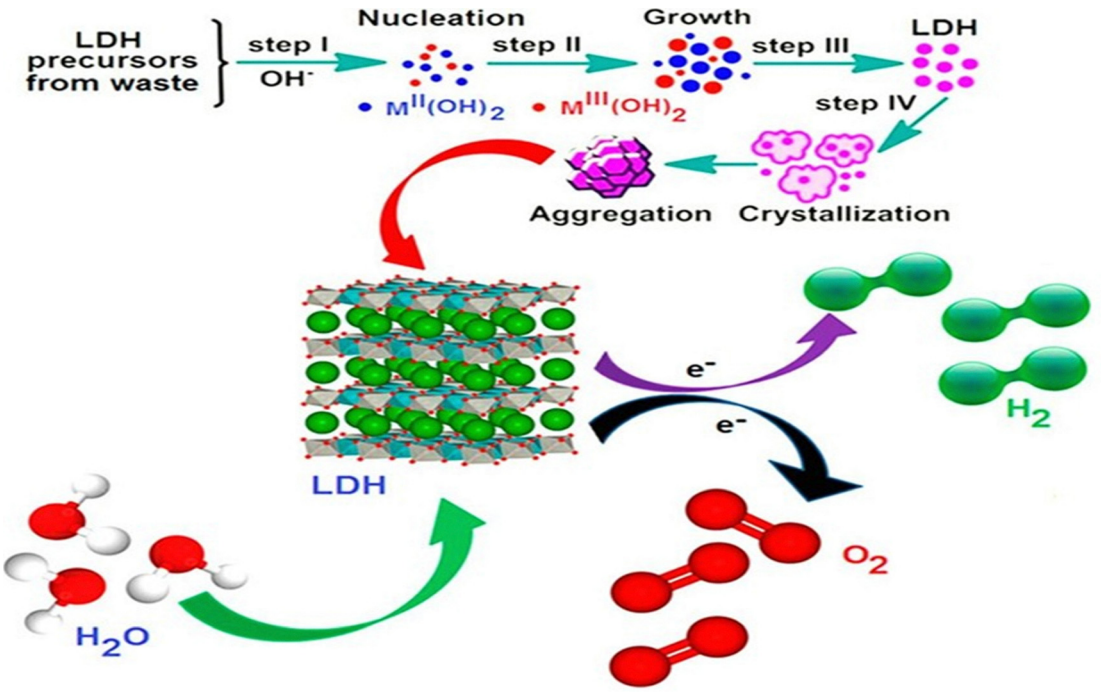

Fig. 3 Schematic representation of the various phases of hydrothermal synthesis of LDHs for green hydrogen production (Adapted with permission from ref. 24©2025, Royal Society of Chemistry and ref. 25©2024, Elsevier).

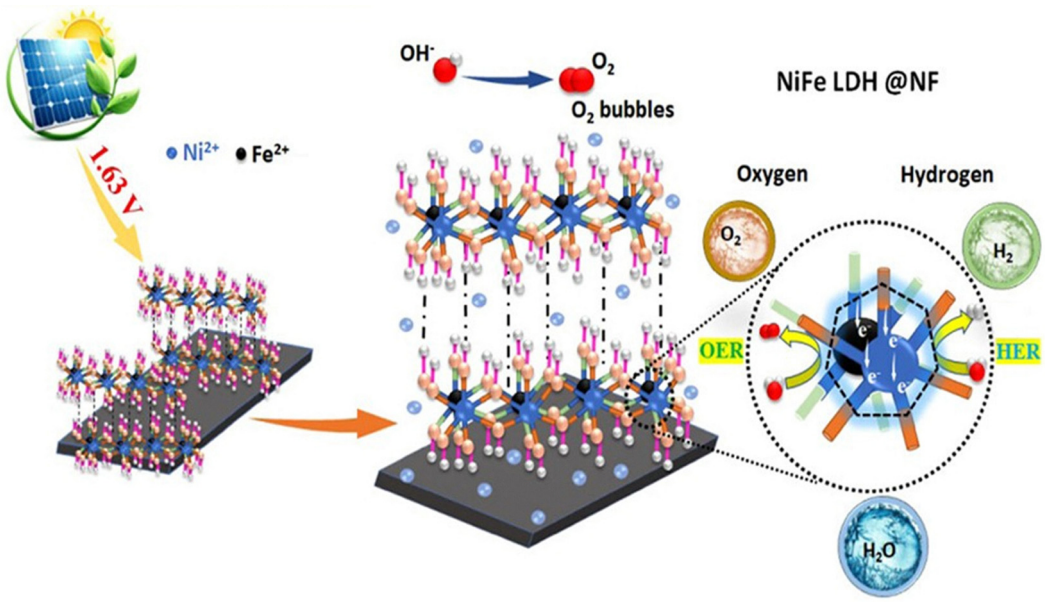

Fig. 4 Schematic depicting a green solvent-free NiFe-LDH for efficient OER and HER (reproduced with permission from ref. 26©2024, The American Chemical Society).

The study reported the synergistic consequences *via* the creation of large electrochemically active sites with well-connected metal ions having nano-spherical architectures. The study also reported that higher OER and HER efficiency could be achieved by optimising the appropriate stoichiometric ratio *viz*, Ni_6Fe_4LDH. According to the linear sweep voltammetric (LSV) curves [Fig. 5(a)], the LDH at the Ni_6Fe_4LDH stoichiometric ratio showed increased OER activity at a current density (10 mA cm^{-2}) in 1 M KOH, with an overpotential of 280 mV [Fig. 5(c)] and a reduced Tafel slope of 116 mV dec^{-1} [Fig. 5(b)], as compared to other electrocatalysts like IrO_2, $Ni(OH)_2$, $Fe(OH)_2$, and NF. Meanwhile, polarisation curves corresponding to HER that were measured between the potential range of −0.4 and 0.0 V were used to assess the HER behaviour of LDH/NF.

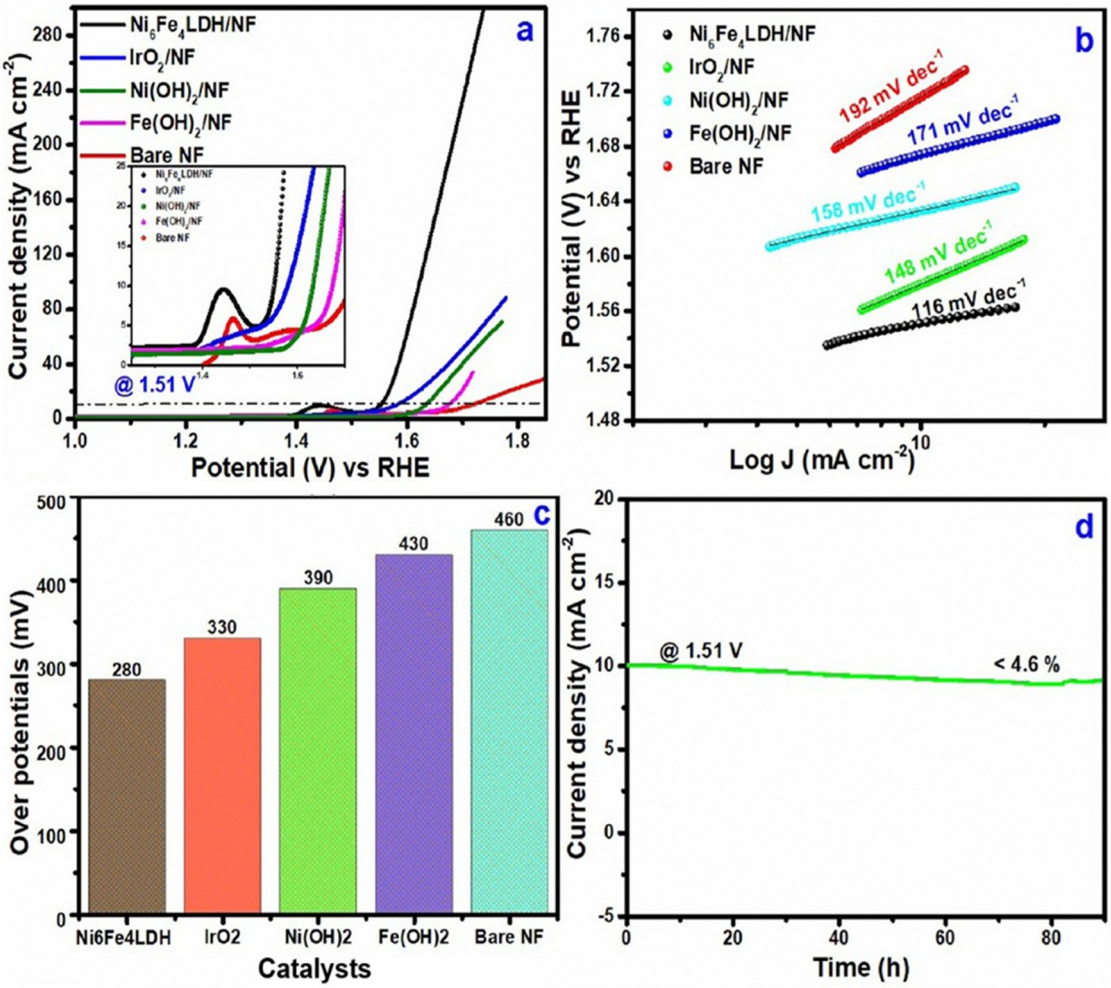

Fig. 5 OER (a) LSV curves (b) Tafel plot (c) overpotentials (at 10 mA cm^{-2}) of Ni_6Fe_4LDH/NF, IrO_2/NF, $Ni(OH)_2$/NF, $Fe(OH)_2$/NF and bare NF (d) current density *vs.* time plot for Ni_6Fe_4LDH/NF (reproduced with permission from ref. 26©2024, The American Chemical Society).

The Ni_6Fe_4 LDH electrode depicted higher catalytic activity than other catalysts, according to the LSV curves shown in Fig. 6(a). Again, with overpotentials of 167 mV [Fig. 6(c)] (at a lower Tafel slope of 112 mV dec^{-1}) [Fig. 6(b)] for the HER, the ideal Ni_6Fe_4LDH ratio achieved 10 mA cm^{-2} (current density) in 1 M KOH. Furthermore, Ni_6Fe_4LDH exhibited remarkable resilience, remaining steady for 90 hours with a slight drop in current density of 4.1 [Fig. 6(d)] and 4.6% [Fig. 5(d)] for the HER and OER, respectively.[26] Interestingly, efficient water electrolysis was achieved in the bifunctional two-electrode configuration of Ni_6Fe_4LDH/NF||Ni_6Fe_4LDH/NF, maintaining a steady current density (= 10 mA cm^{-2}) at a bias of 1.64 V for more than 140 h, with a minor current loss of 3.9% of the current density.

2.3. Waste-derived synthesis routes

The synthesis of red mud-based LDHs for green hydrogen generation leverages the aluminium industry waste as a trivalent metal source (Fe^{3+}, Al^{3+}), combined with divalent metals (*e.g.*, Mg^{2+}), to create LDH-based catalysts for sustainable green hydrogen generation. The synthesis strategy involves the co-precipitation method in which red mud is digested (*e.g.*, with HCl) and mixed with divalent metal sources (*e.g.*, MgO) under controlled pH (9–11) and temperature (70 °C).[27] Optimal conditions have been reported at M^{2+}/M^{3+} molar ratio of 3.0 and ageing at 70 °C for 72 hours.[27] CO_3^{2-} rich environments have been reported to stabilize LDH structures. This synthesis strategy has reported carbonate-intercalated Mg–Fe/Al-LDHs with Fe^{3+} dominance in the hydroxide layers.[27] By transforming red mud into functional LDHs, this approach addresses waste valorisation and clean energy production, aligning with circular economy goals. The different forms of waste-derived LDHs for electrocatalytic water splitting along with their performance metrics have been illustrated in Table 2.

Again, the performance of several recently reported waste-derived LDH-based electrocatalysts with their key features, for OER, HER, and OWS under alkaline and high current density (HCD) conditions have been depicted in Table 3.

2.4. Strategic synthesis of LDH nanoparticles from 2D nanosheets

LDH nanoparticles derived from 2D nanosheets offer unique properties such as high surface area, tunable interlayer spacing, and enhanced catalytic activity. The strategic synthesis approach

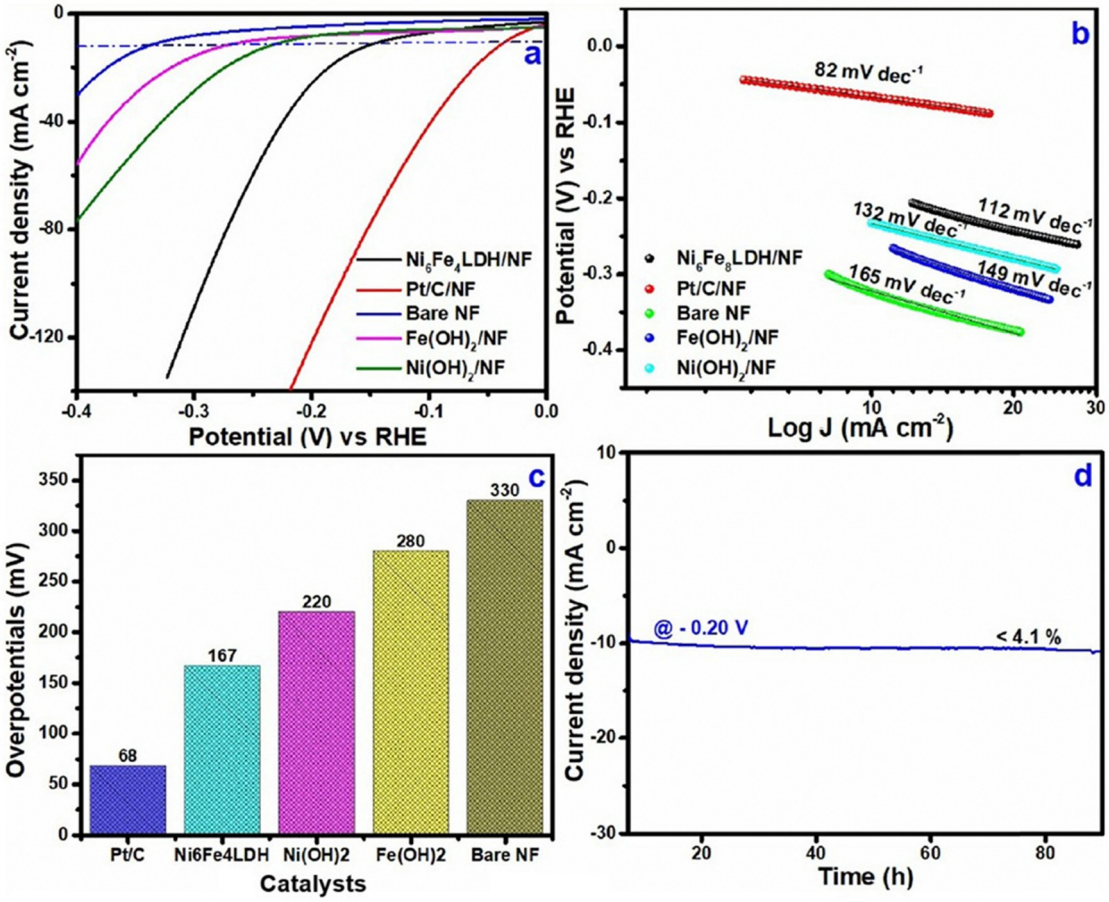

Fig. 6 HER (a) LSV curves (b) Tafel plot (c) overpotentials (at 10 mA cm^{-2}) of Ni_6Fe_4LDH/NF, Pt/C/NF, $Ni(OH)_2$/NF, $Fe(OH)_2$/NF and bare NF (d) current density *vs.* time plot for Ni_6Fe_4LDH/NF (reproduced with permission from ref. 26©2024, The American Chemical Society).

Table 2 Comparison of electrocatalytic water splitting efficiency of waste-derived LDHs

Waste-derived LDHs	Waste sources	Stability; electrolyte	η_j (mV) @ j = 10 mA cm^{-2}		Tafel slope (mV dec^{-1})		Ref.
			OER	HER	OER	HER	
$Ni_{0.5}Mn_{0.3}Co_{0.2}(OH)_2$	Li-ion battery	24 h; 1 M KOH	280	—	6.79	—	28
De-lithiated $Li_{0.4}Ni_{0.5}Co_{0.2}Mn_{0.3}O_2$		80 h; 1 M KOH	236 (η_{20})	—	66	—	29
NiFe-LDH/$Cu(OH)_2$/Cu	Cu-cable wire	24 h @ 20 mA cm^{-2}; 1 M KOH	275 (η_{20}) 390 (η_{100})	—	83	—	30
NiFe-borate LDH/N-doped carbon	C and N-doped C procured from Mangosteen skin	24 h; 1 M KOH	243	—	42.7	—	31
NiFe-borate LDH		—; 1 M KOH	255	—	—	—	
NiFe-C LDH		—; 1 M KOH	274	—	—	—	
NiFe LDH/$(NiFe)S_x$/	CMT procured from Willow	15 h @ 10 mA cm^{-2}	210	169	31	120	32
CMT$(NiFe)S_x$/CMT	catkins	—	300	266	—	—	
NiCaFe-LDH	Bio-waste derived from egg-shell	8 h @ 1.5 mA cm^{-2} and 1.65 V; 0.1 M PO_4^{3-} buffer at pH 7	373	—	13	—	33

η_j: overpotential and current density j (= 10 mA cm^{-2}).

for LDH nanoparticles often involves top-down exfoliation and bottom-up assembly techniques. A study reported the hydrothermal synthesis of defect-rich 3D MgCr-LDHs from their 2D nanosheet counterparts for highly efficient photoelectrochemical water splitting due to reduction in the recombination of photo-induced e^- and h^+ pairs.[39] The relative band position and schematic of charge transfer mechanism of MgCr-LDH nanoparticles for the photocatalytic water splitting is presented in Fig. 7(a).

Fig. 7(b) and (c) presents the plot of current density *vs.* applied potential under light and dark conditions. The material depicted efficient photoelectrochemical properties with a low

Table 3 Performance of various waste-derived LDH-based electrocatalysts for OER, HER, and OWS (overall water splitting) under alkaline and HCD conditions

Electrocatalyst	Reaction	Waste sources	Conditions	Performance metrics	Key features
NiFe-LDH derived from red mud	OER	Red mud (industrial waste)	1 M KOH	Overpotential: ~300 mV @ 10 mA cm^{-2}	High Fe^{3+} content enhances active sites; require conductivity enhancement.[34,35]
MgAlFe-LDH from steel slag	HER	Steel slag	1 M KOH	Overpotential: ~250 mV @ 10 mA cm^{-2}	Effective Fe^{3+}/Al^{3+} utilization; moderate HER performance.[34,36]
NiCo-LDH from mining residues	OWS	Mining residues	Alkaline medium	Overall voltage: 1.58 V @ 10 mA cm^{-2}	Bifunctional activity; improved conductivity *via* Co doping.[35,37]
Ochre-derived LDH	OER	Ochre waste	0.1 M KOH	Overpotential: ~310 mV @ 10 mA cm^{-2}	Defect engineering improves catalytic activity
NiFe-LDH@biochar composite	OWS	Biomass ash	Alkaline medium	Overall voltage: 1.55 V @ 10 mA cm^{-2}	Biochar improves conductivity and stability.[34,36]
ZnCo-LDH from e-waste	HER/ OER	Electronic waste	1 M KOH, HCD	HER overpotential: ~220 mV @ 100 mA cm^{-2} OER overpotential: ~280 mV @ 100 mA cm^{-2}	High durability under HCD; Zn-Co synergy enhances performance.[35,37]
CoCuFe-LDH/graphene	Metal waste	OER/HER	Alkaline	OER onset potential: 1.52 V; HER onset potential: −0.32 V; Tafel slope: 62.8–76.6 mV dec^{-1}	Graphene enhances conductivity; optimized *via* factorial design for HCD stability.[38]

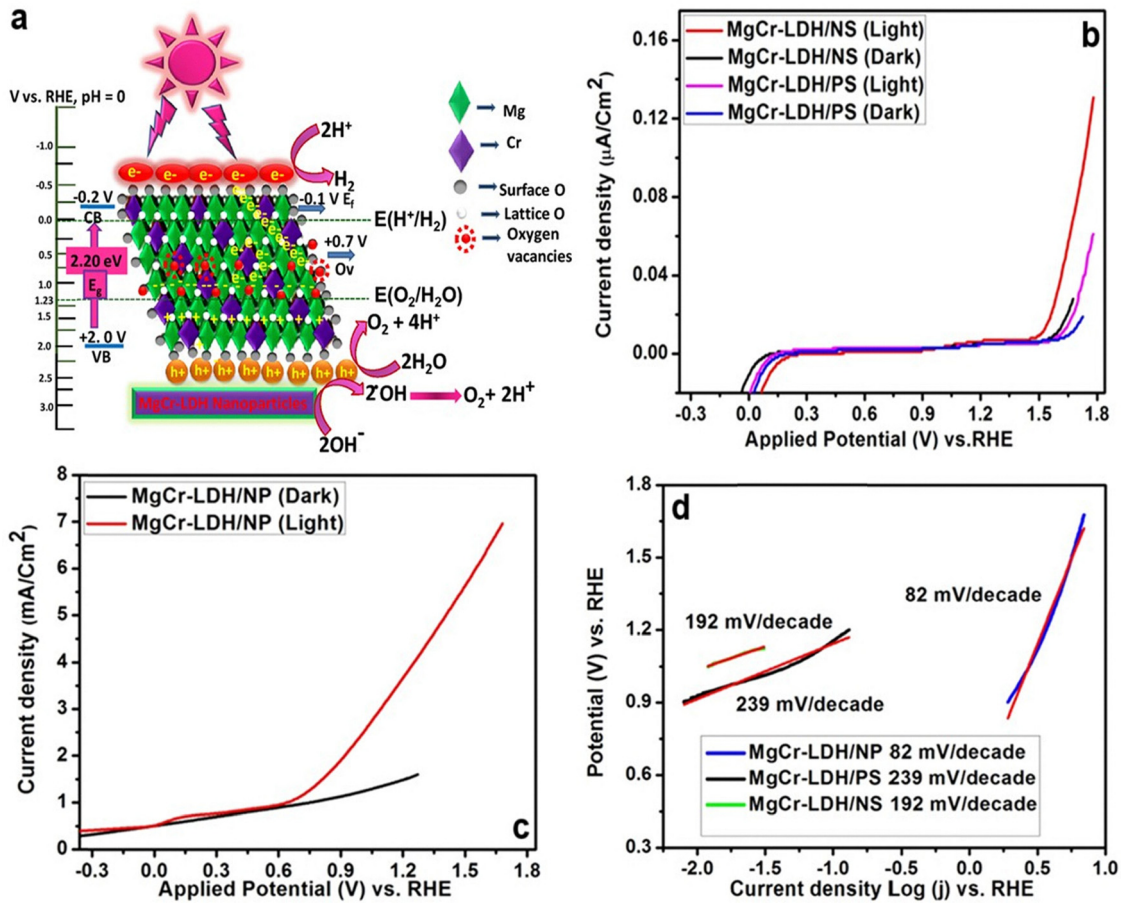

Fig. 7 (a) Schematic representation of the relative band position and charge transfer phenomenon of MgCr-LDH nanoparticles for the photoelectrochemical water splitting. (b) Plot of current density over applied potential (*vs.* RHE) for pristine MgCr-LDH/NS and MgCr-LDH/PS nanoparticles under light and dark. (c) Plot depicting the comparative study of current density over applied potential (*vs.* RHE) for MgCr-LDH/NP under light and dark. (d) Comparative Tafel plots of the pristine LDH over nanoparticles and nanosheets (adapted with permission from ref. 39©2022, Springer Nature; License: CC-BY 4.0).

Tafel slope of 82 mV decade^{-1} and a current density of 6.9 mA cm^{-2}. The comparative Tafel slope of the pristine LDH over nanoparticles and nanosheets could be evident from Fig. 7(d). The study also reported that under visible light, MgCr-LDH nanoparticles presented photocatalytic H_2 evolution of 1315 μmol h^{-1}; which was 1.8 and 4.3 times higher than that of MgCr-LDH nanosheets (726 μmol h^{-1}) and pristine MgCr-LDH (300 μmol h^{-1}), respectively.[39]

2.5. Chemical component adjustment

M^{n+} cations make up the layered architecture with organic or inorganic anionic species along with water molecules within the interlayers.[40] Consequently, expansion properties are exhibited by the LDH owing to its weak interlayer bonding. Studies have reported the creation of numerous 3D nanoarchitectures as a result of tuning the M^{2+}/M^{3+} ratios, varying the choice of metal cation and anion species. The important strategies for chemical component adjustment have been schematically depicted in Fig. 8(a)–(e). Table 4 summarizes chemical component adjustment strategies and their impact on the HER, OER, and stability of LDH-based electrocatalysts.

2.6. Heterojunction construction strategy

These strategies are increasingly used in LDH-based materials to enhance the electrocatalytic performance and address challenges like poor conductivity and slow reaction kinetics in LDHs. The primary strategies for building LDH-based heterojunctions include structural design, band gap engineering, and doping, each targeting improved charge separation and catalytic efficiency. A study reported the generation of core–shell hierarchical structures (Cu_2O@CoFe-LDH) through the creation of p–n heterojunction by coating Cu_2O nanowires with CoFe LDH nanosheets *via in situ* wet-chemical reactions and electrodeposition. The core–shell structure leverages the light-harvesting ability and the built-in electric field at the interface of Cu_2O, enhancing charge separation for water splitting.[48] A separate study reported the generation of Ni_3S_2@V-NiFe-LDH *via* a two-step hydrothermal method, producing a heterostructure with Ni_3S_2 as the base and V-doped NiFe-LDH as the outer layer. The interlaced nanosheets have been reported to increase the surface area and conductivity, critical for OER performance.[49] Meanwhile, a separate study reported the creation of 2D/2D heterojunctions for functionalizing NiCo-LDH/g-C_3N_4. A Z-scheme heterojunction formed by combining 2D NiCo-LDH with g-C_3N_4 nanosheets improved visible-light absorption and charge separation. This structure boosted tetracycline degradation (*via* $^{\bullet}OH$, $O_2^{\bullet-}$, and h^+ species) and hydrogen evolution (451.7 μmol g^{-1} h^{-1}).[50] Band-gap engineering is another important strategy for the generation of staggered-gap heterojunctions in LDHs. In this process, the LDH components have been

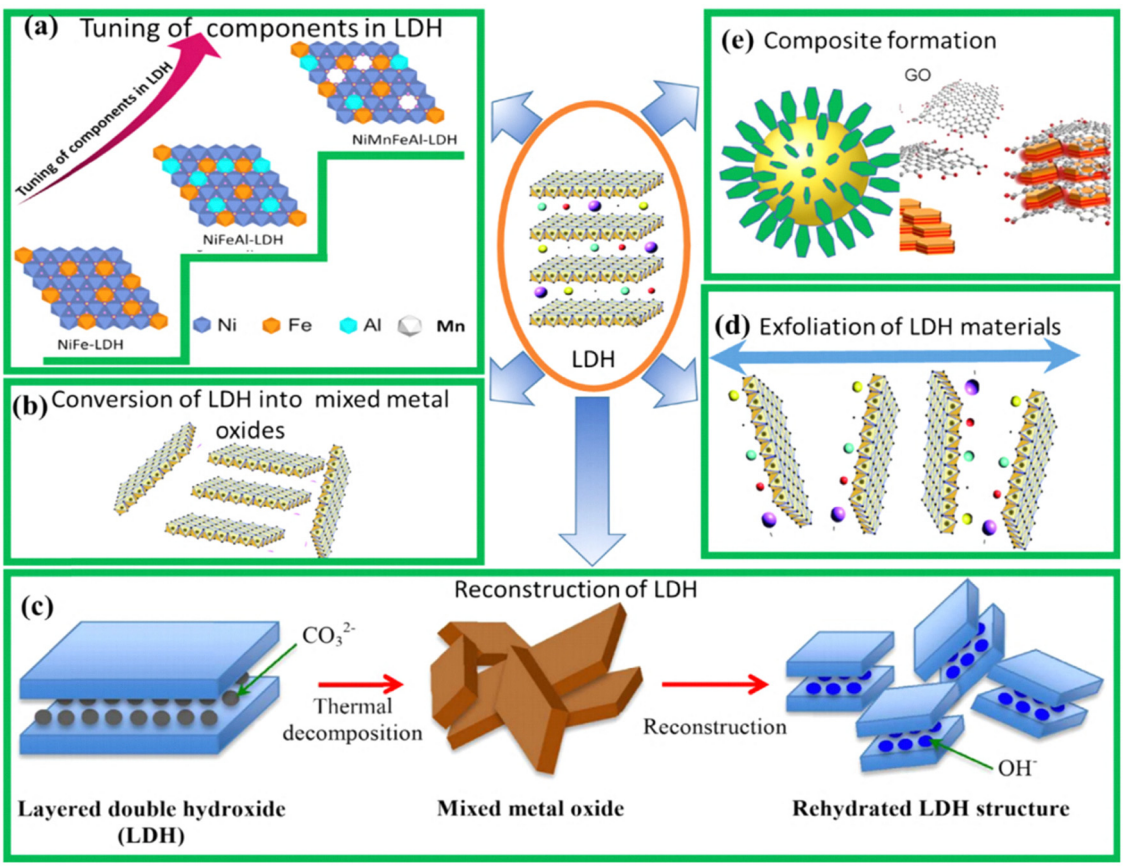

Fig. 8 (a)–(e) Schematic representation of the important strategies for chemical component adjustment in LDHs (adapted with permission from ref. 47©2023, Elsevier).

Table 4 Chemical component adjustment strategies and their impact on the HER, OER, and stability of LDH-based electrocatalysts

Chemical component adjustment	HER activity	OER activity	Current density (mA cm^{-2})	Overpotential (mV)	Tafel slope (mV dec^{-1})	Stability
CoCuFe-LDH/ graphene[41]	Onset voltage: −0.32 V (HER)	Onset voltage: 1.52 V (OER)	10–100	HER: ~220 (100 mA cm^{-2}) OER: ~280 (100 mA cm^{-2})	HER: 76.6 OER: 62.8	>24 h @ 10 mA cm^{-2} (90% retention)
NiFeMn-LDH[42]	—	270 mV @ 10 mA cm^{-2}	10	270	76	>10 h @ 50 mA cm^{-2}
NiFe-LDH/Ni Foam[43]	—	223 mV @ 10 mA cm^{-2}	10	223	48.9	>24 h @ 10 mA cm^{-2}
NiFeV-LDH[44]	—	210 mV @ 10 mA cm^{-2}	10	210	39	>50 h @ 10 mA cm^{-2}
Pt-NiFe-LDH[45]	120 mV @ 10 mA cm^{-2}	204 mV @ 10 mA cm^{-2}	10	HER: 120 OER: 204	HER: 68 OER: 56	>50 h @ 10 mA cm^{-2}
NiLa-LDH[44]	—	209 mV @ 10 mA cm^{-2}	10	209	42	—
NiFe-LDH@Biochar[46]	—	—	10	OWS voltage: 1.55–1.58 V	—	—

reported to tailor their electronic structures, enabling staggered band alignment. A study reported the coupling LDHs with semiconductors like TiO_2 or $BiVO_4$ through the creation of p–n junction that enhance carrier transfer and light-response range.[48,51]

Moreover, doping and electronic modulation has resulted in the synthesis of V-doped NiFe LDH. In this study, V has been introduced into NiFe-LDH by forming an electron transport chain (Ni–O–Fe–O–V–O–Ni), optimizing binding with reaction intermediates and accelerating electron transfer.[49] This dual strategy (heterostructure + doping) reduced OER overpotential to 280 mV at 100 mA cm^{-2}. A comparative study of HER, OER, and OWS based on heterojunction-constructed LDH-based electrocatalysts is presented in Table 5.

2.7. Nanostructure engineering strategy

By integrating nanostructure engineering and electronic tuning, LDH-based catalysts demonstrate exceptional potential for sustainable hydrogen production. Recent advancements in nanostructure engineering strategies have significantly enhanced their catalytic performance through tailored structural and electronic modifications. Recent advancements in nanostructure engineering strategies and their impact on HER and OER are presented in Table 6.

2.8. Quantum-dot modified doping strategies

Quantum-dot (QD) modified doping strategies for LDHs have emerged as a powerful approach to enhance electrocatalytic performance in HER and OER. These strategies leverage the synergistic effects between QDs and LDHs to optimize electronic structures, expose active sites, and improve charge transfer.

A study reported the generation of self-supported Pt_{QDs}@NiFe-LDH through a two-step facile approach involving chemical etching.[61] The synthesis strategy has been schematically presented in Fig. 9(A). The SEM and TEM images of the QD-LDH hybrid presented an orderly arrangement of LDH nanosheets on NF [Fig. 9(B) and (C)]. The XRD of the QD-LDH represented the characteristic peaks showing the doping of QDs into the corresponding NiFe LDH (JCPDS card no. 40-0215). Apart from the characteristic LDH peaks, the XRD peaks at 39.7°, 46.2°, and 67.4° could be attributed to the corresponding peaks (111), (200), and (220) due to the successful doping of Pt_{QDs} onto the LDH (following JCPDS card no. 40-0215) [Fig. 9(D)]. The interplanar spacing was reported to be 0.225 nm, corresponding to (015) plane of NiFe LDH (015) plane of NiFe LDH [Fig. 9(F)]. The dispersion of Pt_{QDs} on the LDH nanosheets could be evident from the spots marked in pink circles in Fig. 9(E) and (F). The average diameter of Pt_{QDs} in Pt_{QDs}@NiFe LDH was reported to be approximately 2.2 nm [Fig. 9(G)]. The EDX mapping revealed the existence of Ni, Fe, O, and Pt in the Pt_{QDs}@NiFe LDH [Fig. 9(H)–(L)]. The loading of Pt by mass has most likely contributed to the abundance of active sites for the HER process.

The HER performance was evaluated at 1 M KOH solution. It was reported that Pt_{QDs}@NiFe LDH exhibited superior HER performance compared to NiFe LDH, Pt/C, and NF [Fig. 10(A) and (B)]. The intrinsic activity [Fig. 10(C)] revealed that

Table 5 Heterojunction construction strategies and their impact on HER, OER, and stability of LDH-based electrocatalysts

Heterojunction construction strategy	HER activity	OER activity	Current density (mA cm^{-2})	Overpotential (mV)	Tafel slope (mV dec^{-1})	Stability
Co(OH)F@CoFe-LDH (core–shell nanorods)[52]	Overpotential: 130 @ 10 mA cm^{-2}	Overpotential: 240 @ 10 mA cm^{-2}	10	OWS voltage: 1.58 V	—	37 h @ 10 mA cm^{-2}
Ni_3S_2@V-NiFe(III)LDH (doped heterostructure)[53]	—	Overpotential: 280 @ 100 mA cm^{-2}	100	280	45.4 (OER)	—
CoMn-LDH (self-assembled hierarchical)[54]	Overpotential: −199 @ 10 mA cm^{-2}	Overpotential: 340 @ 10 mA cm^{-2}	10	—	102 (OER), 128 (HER)	63% retention after 20k cycles
CoMn@CuZnFeS (ternary composite)[54]	Overpotential: −222 @ 10 mA cm^{-2}	Overpotential: 366 @ 10 mA cm^{-2}	10	—	160 (HER)	—
NiFeMn-LDH/OOH-graphene (heterojunction +conductive support)[55]	—	Overpotential: 338 @ 10 mA cm^{-2}	10	—	67 (OER)	—

Table 6 Nanostructure engineering strategies on HER and OER of LDH-based electrocatalysts

Nanostructure engineering strategy	HER activity	OER activity	Current density (mA cm^{-2})	Overpotential (mV)	Tafel slope (mV dec^{-1})	Stability
Pt-NiFe-LDH/CC (sub-nano Pt clusters)[56]	Overpotential: 120 mV @ 10 mA cm^{-2}	Overpotential: 204 mV @ 10 mA cm^{-2}	10	HER: 120 OER: 204	HER: 68 OER: 56	Stable for >50 h under alkaline conditions
CoMn-LDH nanosheets[57]	Overpotential: −199 mV @ 10 mA cm^{-2}	Overpotential: 340 mV @ 10 mA cm^{-2}	10	HER: −199 OER: 340	HER: 128 OER: 102	Retains 63% capacitance after 20 000 cycles
NiFe-LDH/Ni Foam (nanosheet array)[58]	—	Overpotential: 223 mV @ 10 mA cm^{-2}	10	OER: 223	OER: 48.9	Stable for >24 h @ 10 mA cm^{-2}
Gd-Doped NiFe-LDH nanosheets[56]	—	Enhanced OER activity *via* oxygen vacancies and porous morphology	10	~250	—	Stable under alkaline medium
Ni_3S_2@V-NiFe(III) LDH heterostructure[59]	—	Overpotential: 280 mV @ 100 mA cm^{-2}	100	OER: 280	OER: 45.4	—
MgAl-LDH *via* exfoliation[60]	—	Moderate OER activity	10	~300	—	Stable colloidal suspension

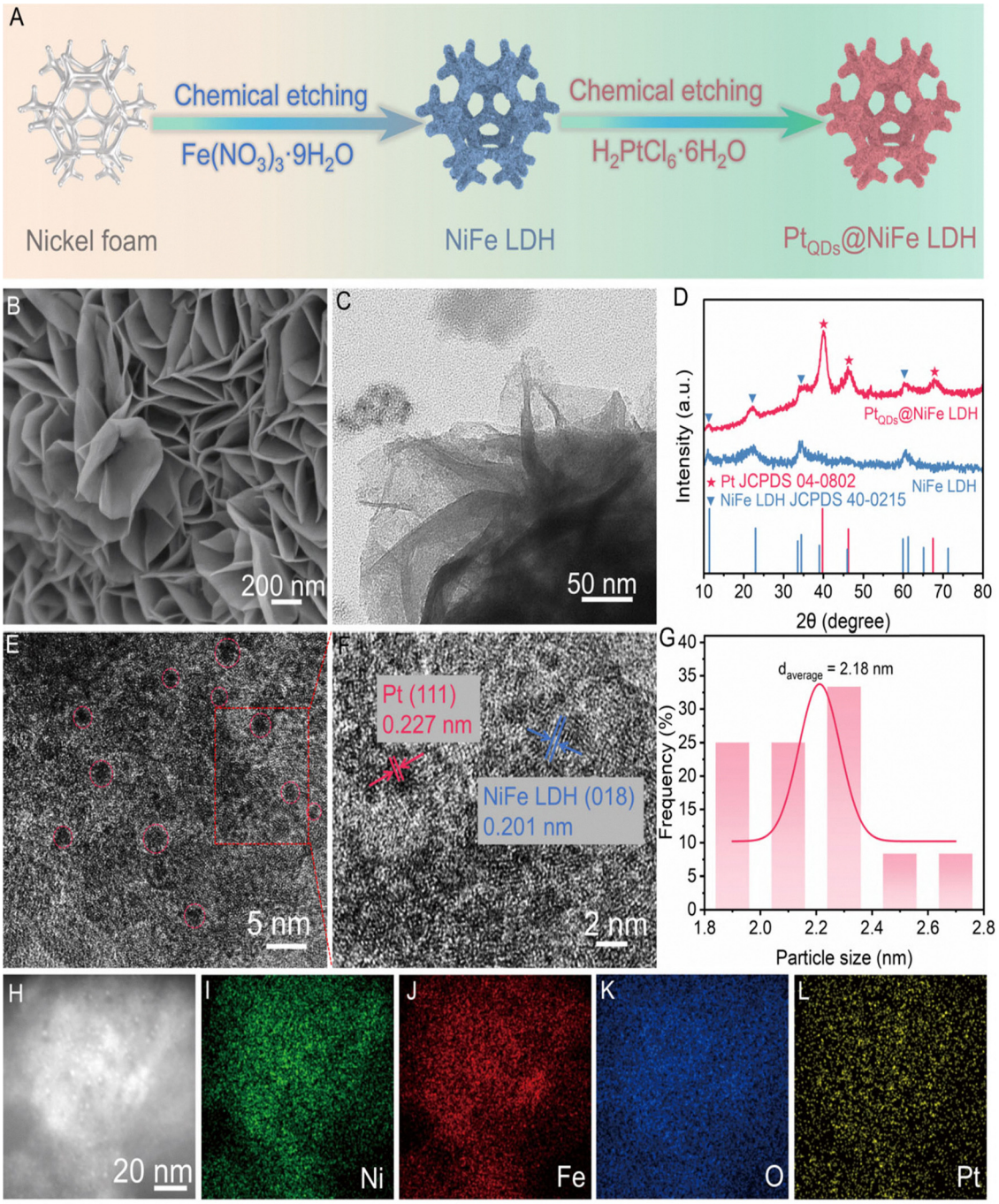

Fig. 9 (A) Schematic illustration of the synthesis of Pt_{QDs}@NiFe LDH, (B) and (C) SEM and HR-TEM images of Pt_{QDs}@NiFe LDH; (D) XRD pattern of Pt_{QDs}@NiFe LDH and NiFe LDH; (E) and (F) HRTEM images of Pt_{QDs}@NiFe LDH; (G) average particle size distribution of Pt_{QDs}; (H)–(L) EDX mapping patterns of various elements within Pt_{QDs}@NiFe LDH (reproduced with permission from ref. 61©OAE publishing, Inc.; License: CC-BY 4.0).

Pt_{QDs}@NiFe LDH possessed highest j_0 (= 4.325 mA cm^{-2}), as compared to the control samples, indicating excellent HER efficiency. The plot of $\Delta\eta/\Delta\log|j|$ for Pt_{QDs}@NiFe LDH *vs.* current density presented a high current density for Pt_{QDs}@NiFe LDH, representing its superior HER efficiency as compared to other catalysts [Fig. 10(D)]. Meanwhile, Fig. 10(E) revealed that Pt_{QDs}@NiFe LDH exhibited the smallest semicircle diameter (= 1.62 Ω), in comparison to other catalysts, depicting its high kinetics associated with charge transfer. Additionally, Pt_{QDs}@NiFe LDH exhibited a double-layer capacitance (C_{dl}) of 55 mF cm^{-2}, which is higher than that of the other control samples observed in this study [Fig. 10(E)]. Fig. 10(G) revealed a higher current density of the Pt_{QDs}@NiFe LDH, in comparison to other catalysts. Fig. 10(H) represents the lowest Tafel slope, as compared to other catalysts, indicating its higher HER efficiency. Thus, the results indicate that Pt_{QDs}@NiFe LDH possess superior

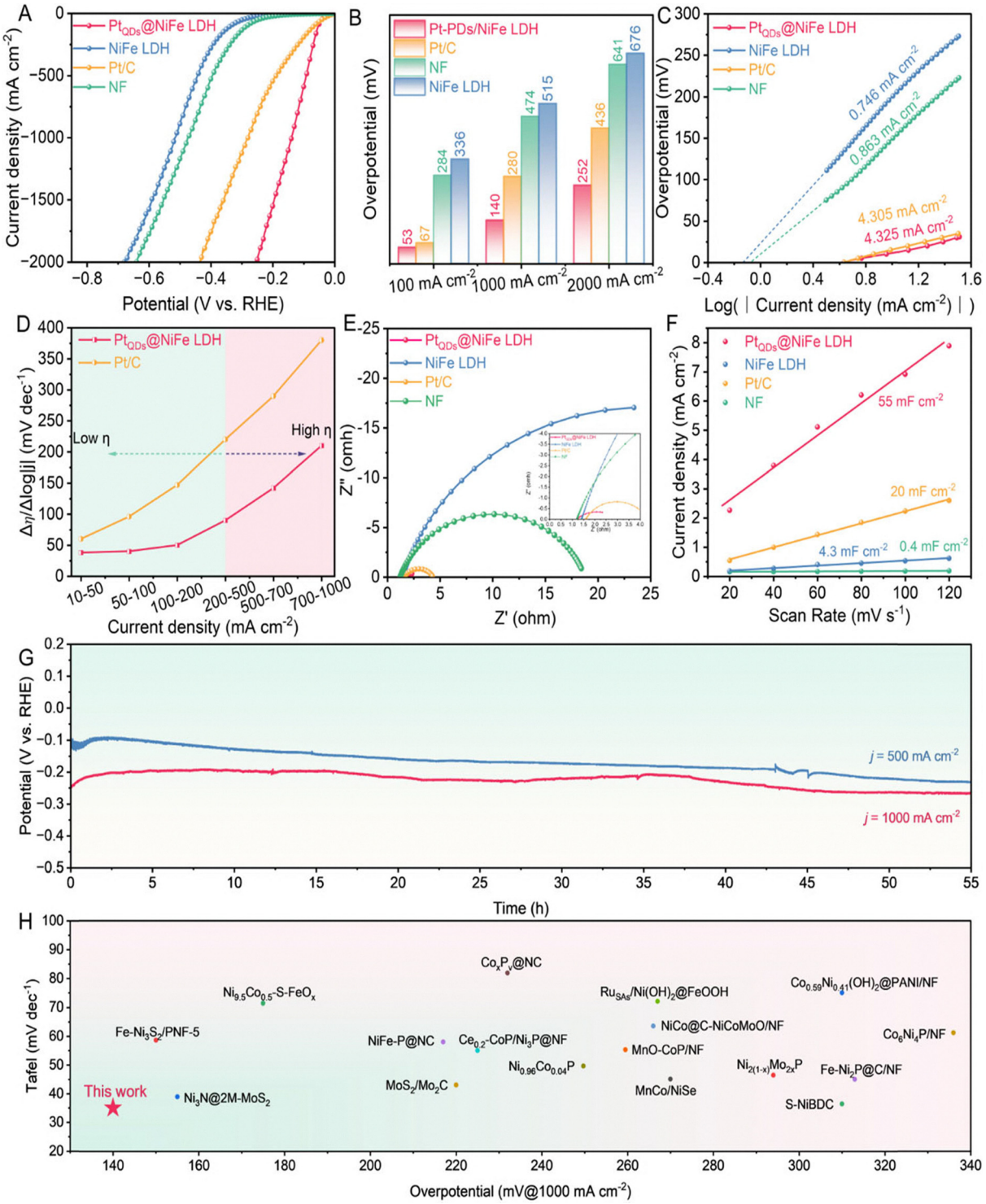

Fig. 10 HER curves (A) LSV plots; (B) plot of overpotential *vs.* log (current density); (C) j_0 of Pt_{QDs}@NiFe LDH some control samples are derived by Tafel plots; (D) Plot of $\Delta\eta/\Delta\log|j|$ *versus* current density ranges; (E) comparative Nyquist plots; (F) plot of current density *vs.* scan rate; (G) potential *vs.* time plots (H) plot of Tafel value *vs.* overpotential of Pt_{QDs}@NiFe LDH over other catalysts (reproduced with permission from ref. 61©OAE publishing, Inc.; License: CC-BY 4.0).

HER efficiency, highlighting their remarkable potential for industrial purposes.

The study also presented the OWS efficiency of the electrocatalysts to expedite their potential for industrial applications. Since, OER is a vital component of OWS, the OER activity of Pt_{QDs}@NiFe LDH-1, Pt_{QDs}@NiFe LDH, Pt_{QDs}@NiFe LDH-5 electrocatalysts, and NiFe LDH precursor was evaluated. Fig. 11(A) and (B) presented highly efficient OER of NiFe LDH over other

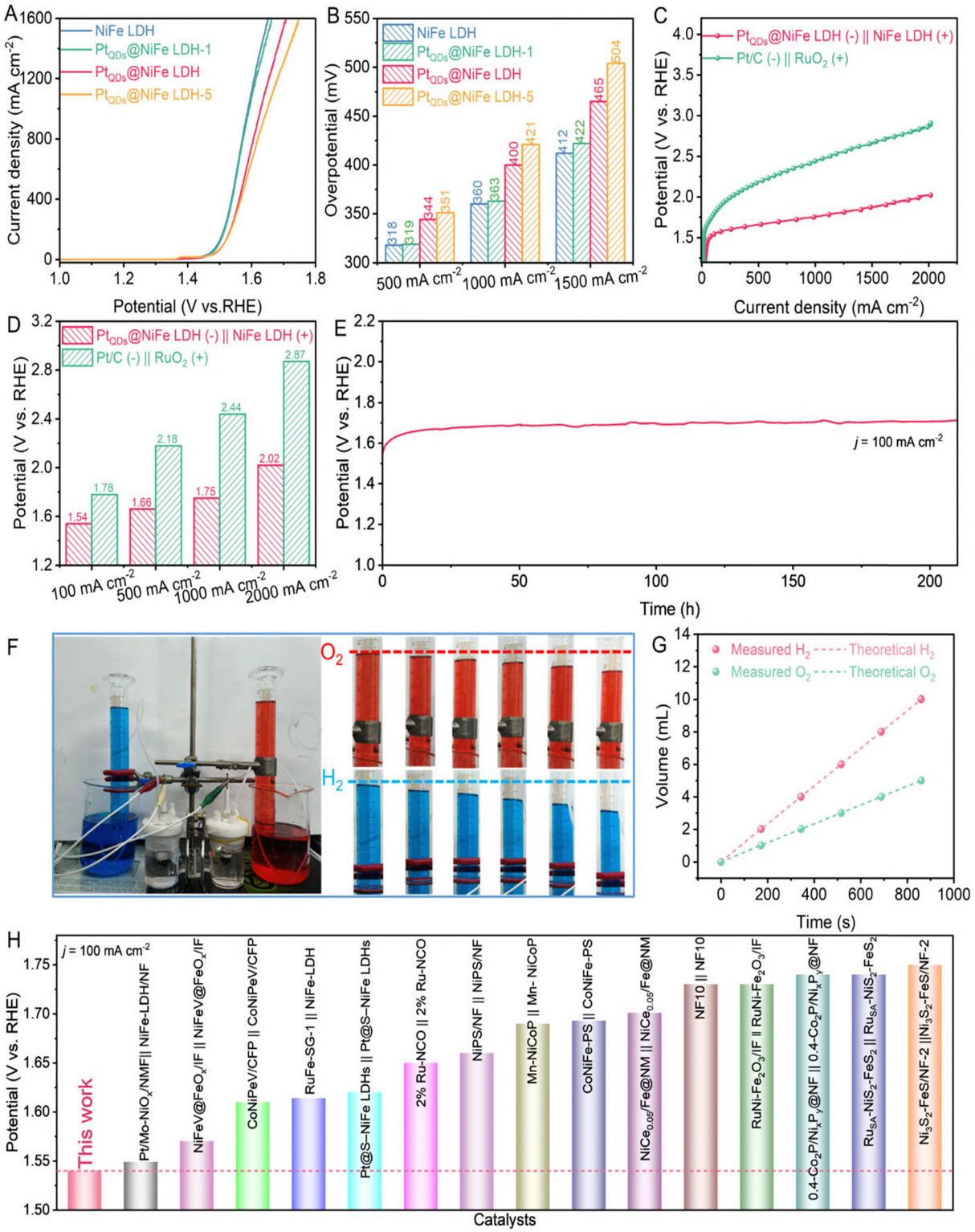

Fig. 11 OWS results; (A) LSV plots; (B) plot depicting comparison of overpotentials at different current densities; (C) potential *vs.* current density plots Pt$_{QDs}$@NiFe LDH (−)||NiFe LDH (+) and Pt/C (−)||RuO$_2$; (D) plot of potential (cell voltage) *vs.* current density (E) potential *vs.* time plot depicting stability in OWS process; (F) snapshots representing the OWS experimental set up and extent of gas collection at different instances; (G) plot depicting measured volume of H_2 or O_2 against theoretically produced H_2 or O_2 w.r.t. time; (H) potential comparison of Pt$_{QDs}$@NiFe LDH (−)||NiFe LDH (+) over other reported electrocatalysts (reproduced with permission from ref. 61©OAE publishing, Inc.; License: CC-BY 4.0).

Table 7 Quantum dot modified and doping strategies for LDH-Based materials in HER and OER processes

Quantum dot modification strategy	HER activity	OER activity	Current density (mA cm^{-2})	Overpotential (mV)	Tafel slope (mV dec^{-1})	Stability
Pt QDs@NiFe LDH[61–63]	Overpotential: 92 mV @ 500 mA cm^{-2}, 252 mV @ 2000 mA cm^{-2}	OWS voltage: 1.66 V @ 500 mA cm^{-2}, 2.02 V @ 2000 mA cm^{-2}	500–2000	HER: 92–252 OWS: 1.66–2.02 V	HER: 35	Stable for >200 h under industrial conditions
CdMoSe-QD/NiV-LDH (S-scheme heterojunction)[64]	Photocatalytic H_2 production rate: 7.36% ACE	Photocatalytic H_2O_2 production rate: 1.67% SCC	—	—	—	Enhanced photocatalytic stability due to delayed recombination of excitons
Pt QDs@S-NiFe LDH (Sulfur-doped)[62,63]	Overpotential: 53 mV @ 100 mA cm^{-2}, 140 mV @ 1000 mA cm^{-2}, 252 mV @ 2000 mA cm^{-2}	OWS voltage: 1.54 V @ 100 mA cm^{-2}, 1.75 V @ 1000 mA cm^{-2}	100–2000	HER: 53–252 OWS voltage: 1.54–1.75 V	HER: ~40	Stable for >55 h at high current densities
Carbon QD/NiFe-LDH Composite[65]	—	Overpotential: ~300 mV @ moderate current densities	Moderate	~300	—	Stable under alkaline conditions
ZnS QDs-ZnAl-LDH[64,66]	Solar water splitting efficiency	Photocatalytic hydrogen evolution	—	—	—	Enhanced photocatalytic durability due to quantum confinement effect

Pt_{QDs} loaded samples due to the exceptionally low overpotential of NiFe LDH over other samples. Moreover, a two-electrode system was constructed involving Pt_{QDs}@NiFe LDH, having high HER (as cathode) and NiFe LDH having highly efficient OER (as anode), represented by Pt_{QDs}@NiFe LDH (−)‖NiFe LDH (+), for evaluation of OWS efficiency. Separate two-electrode systems were assembled and as Pt/C (−)‖RuO_2 (+) for comparative study.

Fig. 11(C) and (D) exhibited superior OWS efficiency with high current density of Pt_{QDs}@NiFe LDH (−)‖NiFe LDH (+) electrode system over Pt/C (−)‖RuO_2 (+). Pt_{QDs}@NiFe LDH (−)‖NiFe LDH (+) electrolyzer only needed 1.54, 1.75, and 2.02 V of applied voltages to achieve 100, 1000, and 2000 mA cm^{-2}, respectively, which is much higher than that observed for Pt/C (−)‖RuO_2 (+) systems, thereby depicting highly efficient OWS process with Pt_{QDs}@NiFe LDH (−)‖NiFe LDH (+). The electrode system, Pt_{QDs}@NiFe LDH (−)‖NiFe LDH (+), also presented high stability at 100 mA cm^{-2} for 200 h [Fig. 11(E)]. Fig. 11(F) presented the snapshots representing the OWS experimental set-up of Pt_{QDs}@NiFe LDH (−)‖NiFe LDH (+) system and the extent of gas collection at different instances. Fig. 11(G) highlighted the plot depicting measured volume of H_2 or O_2 against the theoretically produced H_2 or O_2 w.r.t. time. It was reported that the ratio of $H_2 : O_2$ in OWS = 2 : 1, representing the Faraday efficiency (FE) ~ 100%, depicting an excellent OWS catalytic activity with Pt_{QDs}@NiFe LDH (−)‖NiFe LDH (+) systems over other reported electrocatalysts. The encouraging OWS results [Fig. 11(H)] highlight the significant potential of Pt_{QDs}@NiFe LDH (−)‖NiFe LDH (+) electrolyzing systems for industrial uses over other commercial catalytic systems. Moreover, Table 7 summarizes several quantum dot modified and doping strategies for LDH-based materials and their impact on the HER, OER, and stability of LDH-based electrocatalysts.

3. LDH-based materials for alkaline seawater and freshwater splitting

Both alkaline freshwater and seawater splitting have seen major advances in catalyst design, with HER, OER, and OWS now possible at low overpotentials and high current densities. In seawater, suppressing side reactions (especially chlorine evolution reaction; CER) and ensuring catalyst stability are key, with defect engineering and single-atom strategies showing great promise for sustainable hydrogen production. LDH-based materials are pivotal for the future of water splitting in both seawater and freshwater, offering a rare combination of low cost, tunable chemistry, high activity, and adaptability to harsh environments. Actually, in sea water electrolysis competition between OER and Cl^- oxidation (CER) occurs, which results in anodic potential window overlapping the chlorine-evolution reaction, so LDHs could either produce O_2 or oxidize Cl^- to Cl_2/HOCl/OCl^-; even small shifts in local pH/overpotential could flip selectivity toward chlorine chemistry, which rapidly could damage electrode materials. That is why, some engineered NiFe-LDH formulations have been reported to be

Table 8 Comparative evaluation of OER, HER and OWS involving seawater under different conditions

Electrocatalyst	Conditions	Reaction	Current density (mA cm^{-2})	Overpotential (mV)	Tafel dlope (mV dec^{-1})	Stability
MgAlCe-LDH/β-Ni$(OH)_2$/Ni foam[72]	Natural seawater (alkaline)	OER	10	80	—	25 h @ 15 mA cm^{-2}
		HER	10	337	—	
		OWS	10	1.42 V (cell voltage)	—	
ZnFe LDH@NiCoS/NF[73]	Alkaline seawater (1 M KOH + seawater)	OER	10	284.8	81.5	50 h @ 10 mA cm^{-2}
		HER	10	246.3	74.6	
		OWS	10	1.593 V (cell voltage)	—	
NiFe-LDH[74]	Artificial alkaline seawater (KOH + 0.5 M NaCl)	OWS	600 (HCD)	—	—	100 h @ 600 mA cm^{-2}

more selective for OER in alkalinized seawater and could suppress CER at moderate potentials, but the selectivity window is narrow and system-level chloride control is generally required for long lifetimes.[67] Impurities, scaling, fouling, and trace poisons present in sea-water could also impact the efficiency of LDHs for OER processes. Natural organics and microbes in seawater could also get adsorbed to electrodes and membranes, increasing overpotentials and promoting heterogeneous reactions that can degrade polymers or catalysts. Antifouling coatings and pretreatment could reduce but don't eliminate this risk. Moreover, minor ions (Cu^{2+}, Fe^{3+}, Br^-) and suspended solids could poison active sites or catalyze unwanted side reactions over time, changing catalytic behaviour and accelerating degradation.

Inspite of these shortcomings, LDHs are among the best alkaline OER catalysts as it could self-reconstruct into active oxyhydroxide phases and have high intrinsic activity. In order to overcome these limitations, practical mitigation strategies should include using bipolar membranes (BPM) or three-compartment designs with LDHs so the anolyte is alkaline and chloride could be excluded from the anode compartment, substantially reducing CER risk.[68] Another, strategy could be using a central saline compartment with selective ion traps or a buffer layer for reducing direct Cl^- flux to the anode.[69–71] Moreover, LDH surface/interlayer engineering (doping, phosphate intercalation, protective shells) along with operational pretreatment could manage scaling.

On the other hand, a comparative cost perspective on "green" synthesis of LDHs for OER reveals that conventional hydrothermal methods, though widely employed, are resource-intensive owing to their reliance on high-temperature (120–200 °C) and high-pressure conditions, long reaction durations, and the use of significant volumes of solvents, all of which raise both capital and operational expenditure. In contrast, solvent-free approaches such as mechanochemical grinding, solid-state reactions, and molten-salt methods have been significantly reducing synthesis costs by eliminating solvent purchase and recovery, shortening reaction times, and minimizing energy demand. These strategies could not only lower the overall energy footprint but also decrease environmental management costs associated with solvent disposal, aligning with the principles of green chemistry. Nonetheless, challenges remain regarding large-scale morphology control and reproducibility, which hydrothermal systems currently address more effectively. Therefore, while solvent-free methods are economically and environmentally advantageous for sustainable LDH production, further optimization is needed to achieve industrial scalability. Continued innovation in their design and hybridization is expected to further unlock their potential for sustainable hydrogen production. A comparative table (Table 8) of recently reported LDH-based electrocatalysts for HER, OER and OWS involving seawater under natural alkaline, artificial alkaline and artificial alkaline with added NaCl is listed herein.

A comprehensive comparison of LDH-based materials for alkaline seawater and freshwater splitting, based on recent studies, has been presented in Table 9. Alkaline conditions suppress chlorine evolution ($Cl^- \rightarrow ClO^-/ClO_3^-$) by widening the potential gap between OER and the chlorine evolution reaction (CER).

A comparative analysis of recently reported LDH-based electrocatalysts for OWS and OER involving alkaline freshwater, simulated seawater, alkaline seawater, alkaline industrial sewage water has been summarized in Table 10.

4. Mechanism of OER, HER and OWS involving LDH-based materials

The mechanism of OER proceeds through three typical mechanisms under alkaline conditions, *i.e.* adsorbate evolution

Table 9 Performance comparison of LDH-based electrocatalysts under alkaline seawater and freshwater conditions with key features

Catalyst	Electrolyte	Overpotential (mV) @ 10 mA cm^{-2}	Cell voltage (V) @ 10 mA cm^{-2}	Stability	Key features
Se-FeCo-LDH[75]	Alkaline seawater	OER: 229 @ 100 mA cm^{-2}	1.491	245 h @ 10 mA cm^{-2}	Partial selenization forms an anion barrier to repel Cl^-, improving durability.
NiCo-LDH-[76]	Freshwater (1 M KOH)	HER: 180 OER: 317	—	20 h @ 10 mA cm^{-2}	Alkali treatment creates metal vacancies, improving HER/OER activity.
Ru/Fe-NiCr-LDH[77]	Freshwater (alkaline)	—	1.6–2.0 V @ 262.5 mA cm^{-2}	Scalable AEM WE system	Ru/Fe doping optimized electronic structure for efficient H* and OOH* steps.

Table 10 Comparative analysis of LDH-based electrocatalysts for OWS and OER involving alkaline freshwater, simulated seawater, alkaline seawater, alkaline industrial sewage water along with its performance metrics

Catalyst	Conditions	Reaction	Current density (mA cm^{-2})	Overpotential (mV)	Tafel slope (mV dec^{-1})	Stability
NiFeCrCo LDH[78]	Alkaline freshwater (1 M KOH)	OWS	10/100	Overall voltage = 1.42 V/1.54 V	—	>120 h (simulated seawater)
	Simulated seawater (1 M KOH + NaCl)	OWS	10/100	Overall voltage = 1.57 V/1.71 V	—	>120 h
NiCo@NiFe LDH[79]	Alkaline seawater (1 M KOH + seawater)	OER	100/500	222/266	46.1 (OER)	>100 h @ 500 mA cm^{-2}
NiCoFe-LDH[80]	Alkaline industrial sewage (6 M KOH)	OER	10/500	274 @ 10 1.68 V @ 500	—	Stable at industrial currents
FeOOH/CoFe LDH[81]	Simulated seawater (1 M KOH + 0.5 M NaCl)	OER	100/400	320 @ 400 (25 °C) 257 @ 400 (60 °C)	—	300 h @ 100 mA cm^{-2}
NiTe@NiFe-LDH[82]	Alkaline seawater (1 M KOH + seawater)	OER	100/500	277/359	68.66 (OER)	50 h @ 100 mA cm^{-2}

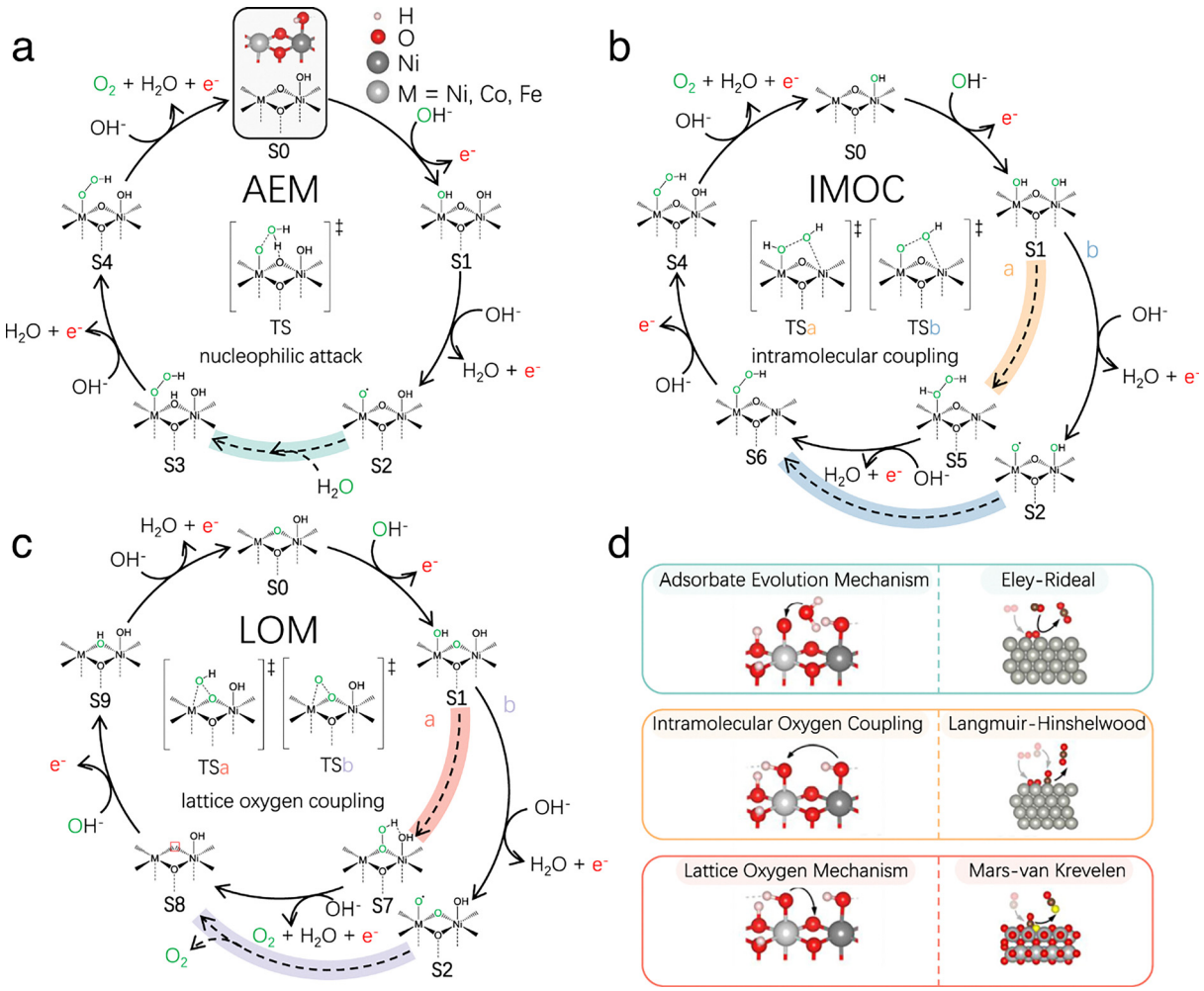

Fig. 12 Mechanistic pathways of OER involving LDH-based materials in alkaline conditions, (a) AEM, (b) IMOC, (c) LOM. Various states involved in the reaction pathways have been designated by S_n and O–O coupling is depicted by dashed lines and highlighted (in Gray). The transition state (TS) of the coupling step is presented in the middle of each cyclic route (d) identification of different reaction models involved in AEM, IMOC and LOM, respectively, in the case of OER with LDH-based materials (reproduced with permission from ref. 83©2025, Springer Nature; License-CC-BY-4.0).

mechanism (AEM), intramolecular oxygen coupling (IMOC) and lattice oxygen mechanism (LOM). Each of the mechanisms proceeds through four (electrochemical) steps and one coupling (O–O) step. The skeletal framework of active sites depicts only the dual metal centres comprising of transition metal sites linked by two O^{latt} lattice oxygen atoms [Fig. 12(a)–(c)]. A recent study[83] demonstrated that the AEM pathway proceeds through the formation of Ni(M)OOH, through the involvement of O–O

coupling, through the generation of $O^{\bullet}*$ radical [Fig. 12(a)]. During the AEM process, oxidation of OH^- leading to the adsorbed OH*, followed by its deprotonation to $O^{\bullet}*$. The reactive species $O^{\bullet}*$ synergistically attack an H_2O along with the neighbouring O^{latt}, generating *OOH and $O^{latt}H$ species, delivering O–O coupling step. This step follows deprotonation, leading to the recovery of O^{latt} from $O^{latt}H$ and O_2 from *OOH subsequently.

The IMOC route associated with Ni(M)OOH [Fig. 12(b)] has been reported to proceed through the aggregation of the adsorbates lying in the vicinity to generate O–O coupling, leading to the formation of two branches. In branch (a) O–O coupling occur between two neighbouring *OH (S1), while in branch (b), associated with step S2, $O^{\bullet}*$ is formed at first, followed by the generation of O–O bond and subsequently –OOH respectively.

The LOM has been reported to exhibit contrasting route in comparison to the AEM and IMOC, coupling the O^{latt} bridging with the vicinity adsorbate to generate O–O coupling [Fig. 12(c)]. There are also two branches in LOM process. In branch (a), O^{latt} has been reported to couple with *OH in S1 step, while in branch (b) O^{latt} reportedly coupled to $O^{\bullet}*$ after S2 is generated. The utilized O^{latt} is subsequently recovered by electro-oxidation and OH^- deprotonation.

The LOM directly engages oxygen atoms from the LDH lattice, thereby bypassing the conventional scaling relationship between *O and *OOH intermediates. This often results in reduced overpotentials and improved catalytic performance. For LOM to proceed effectively, the LDH lattice framework must enable reversible oxygen extraction and replenishment while preserving structural integrity.[83]

LDHs consist of positively charged brucite-like sheets, where divalent and trivalent metal cations are coordinated to hydroxyl groups.[22,23,83] These layers are interspaced with charge-balancing anions and water molecules, endowing the material with intrinsic structural flexibility. Such a configuration renders LDHs more ''breathable'' compared to rigid oxide frameworks like rutile or perovskite.

The flexibility of the LDH lattice is central to promoting LOM. Dynamic metal–oxygen coordination allows local distortion of M–O octahedra during redox cycling, which in turn supports the formation and recombination of oxygen vacancies. This structural adaptability enables lattice oxygen to actively participate in the oxygen evolution reaction (OER).

Additionally, the layered structure could accommodate non-stoichiometry, as interlayer anions and hydroxide sheets mitigate the strain associated with oxygen extraction, thus preventing structural collapse and facilitating reversible lattice oxygen participation.

Moreover, lattice flexibility enhances metal-oxygen covalency, in transition metal based LDHs, by improving orbital overlap between O 2p and metal 3d states. This electronic feature strongly favours lattice oxygen redox processes. LDHs could also undergo localized strain relaxation, such as expansion or compression around catalytic sites, thereby lowering the energy barrier for oxygen release and accelerating LOM pathways.[83]

Finally, the interlayer constituents play a vital role in structural recovery. After lattice oxygen involvement in OER, intercalated anions (*e.g.*, OH^-, CO_3^{2-}) and water molecules assist in re-oxidizing the framework, ensuring sustained catalytic activity. Collectively, these structural and electronic attributes make LDHs particularly well-suited as efficient and durable catalysts operating *via* the lattice oxygen mechanism.

The study further reported that the O–O coupling steps in AEM process follow the Eley–Rideal (ER) model and involve adsorbed $O^{\bullet}*$ reacting with a H_2O molecule in the electrolyte [Fig. 12(d)]. The O–O coupling steps in the IMOC process have been reported to follow the Langmuir–Hinshelwood (LH) model, involving the adsorbed reactants only. The O^{latt} of the catalyst is consumed O–O coupling in the Mars–van Krevelen (MvK) model, being followed by the LOM pathway during the OER process.

LDHs are emerging as highly effective and tunable electrocatalysts for HER, especially in alkaline media. Their unique structure, compositional flexibility, and ability to host multiple active sites make them attractive for sustainable hydrogen production.[84–86] The fundamental HER pathways in alkaline solution proceed through two main steps. The first step is regarded as Volmer step, in which water molecule adsorption and dissociation on metal sites occur, producing adsorbed hydrogen (H*) and hydroxide (OH^-).

$$H_2O + e^- \rightarrow H^* + OH^- \quad (1)$$

The second step involves Heyrovsky step (electrochemical desorption), in which an adsorbed hydrogen reacts with another water molecule and an electron to produce hydrogen gas and hydroxide

$$H^* + H_2O + e^- \rightarrow H_2 + OH^- \quad (2)$$

The third step involves the chemical desorption, or the Tafel step, in which the two adsorbed hydrogen atoms combine to form hydrogen gas.

$$2H^* \rightarrow H_2 \quad (3)$$

The rate-determining step could vary depending on the type of LDH-based catalyst and conditions, but in alkaline media, the initial water dissociation (Volmer step) is often the slowest and most critical. LDHs could facilitate the Volmer step by providing optimal binding sites for water molecules and stabilizing the reaction intermediates. The Heyrovsky/Tafel steps are generally accelerated by the synergistic interaction between metal centers and the optimized surface electronic structure, which lowers the energy barrier for hydrogen desorption. The overall HER efficiency could be determined by the balance between water dissociation ability and hydrogen binding strength-both of which could be tuned *via* LDH composition and structure. Doping, defect engineering, and hybrid nanostructures could enhance their performance, making them highly promising for scalable hydrogen production in alkaline environments.

LDHs are among the most promising earth-abundant electrocatalysts for OWS, efficiently catalyzing both the HER and OER in alkaline media. Their unique layered structure, tunable

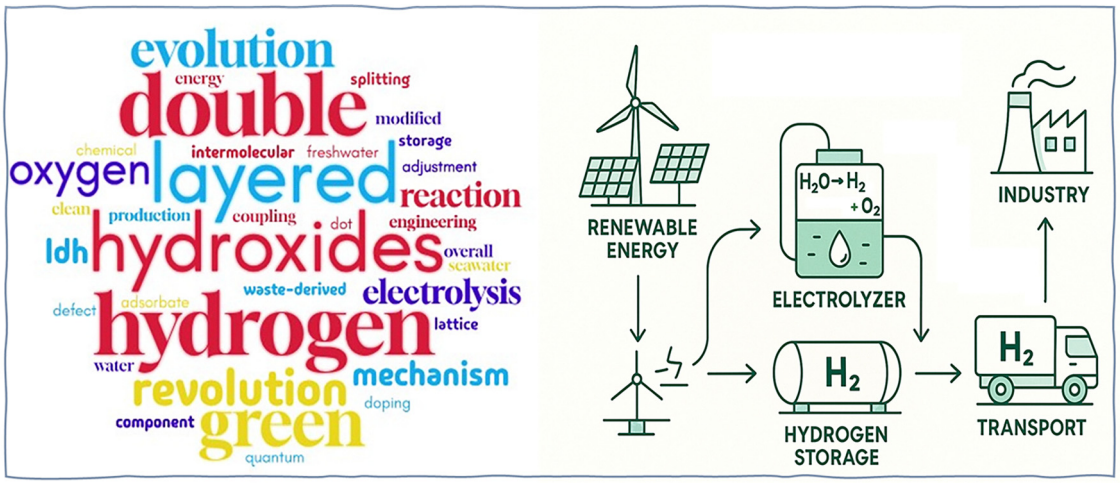

Fig. 13 Schematic representation of the concept of a green hydrogen ecosystem with LDH-based materials.

composition, and ability to host multiple active sites underpin their high performance and versatility. OWS consists of two half-reactions:

HER (at cathode)

$$2H_2O + 2e^- \rightarrow H_2 + 2OH^- \quad (4)$$

OER (at anode)

$$4OH^- \rightarrow 2H_2O + O_2 + 4e^- \quad (5)$$

In an LDH-based electrolyzer, the same or similar LDH material can serve as both anode and cathode, enabling bifunctional catalysis for OWS. The HER pathways follow the Volmer step, Heyrovsky step and Tafel step in a successive manner. Similarly, OER pathways include adsorption of OH^- (OH^- binding to the transition metal centers in the LDH), formation of OOH* intermediates (stepwise oxidation of adsorbed OH^- to form O*, OOH*, and finally releasing O_2). Finally, the redox-active metals (*e.g.*, Ni^{2+}/Ni^{3+}, Fe^{2+}/Fe^{3+}) facilitate multi-electron transfer and stabilize reaction intermediates.

5. LDHs and green hydrogen economy

The green hydrogen economy is a transformative framework for decarbonizing energy systems by leveraging green hydrogen's versatility as a clean energy carrier and storage medium. The hydrogen economy is essential to mitigate the challenges associated with climate change, energy security, thereby fostering economic growth. The green hydrogen economy involving LDHs integrates advanced catalytic materials with renewable energy systems to enable efficient and sustainable hydrogen production. In the quest for a sustainable and low-carbon future, the world is turning its attention to innovative solutions, and one such promising avenue is the development of a green hydrogen ecosystem. A schematic representation of the concept of a green hydrogen ecosystem with LDH-based materials is depicted in Fig. 13. Green hydrogen, however, is produced using renewable energy sources, making it a key player in the transition towards a greener and more sustainable energy landscape. LDHs are emerging as cornerstone materials in advancing the green hydrogen economy due to their structural flexibility, cost-effectiveness, and catalytic efficiency. LDHs excel in driving the OER and HER processes, which are regarded as critical steps in water electrolysis due to their low overpotentials, the existence of defect states and bifunctional catalytic properties.

A study reported that NiFe-LDH hollow microspheres synthesized *via* a SiO_2-templated method achieved an ultra-low OER onset overpotential of 239 mV at 10 mA cm^{-2}, outperforming commercial Ir/C catalysts. The hierarchical structure has been reported to enhance active site exposure and ion transport, yielding a current density of 71.69 mA cm^{-2} at 300 mV overpotential and stability over prolonged operation.[87] A separate study also reported that exfoliated CoAl-LDH nanosheets with oxygen vacancies reduced the coordination numbers (Co–O from 4.2 to 3.7) and enhanced conductivity, enabling stable OER performance for 110 hours.[88] A separate study also reported the integration of LDHs with transition metal dichalcogenides (TMDs, *e.g.*, MoS_2) enhanced the HER/OER synergy due to tunable metal centers, exposed edge sites and layered structure. LDH-TMD together could enable efficient overall water splitting, particularly in seawater electrolysis, by mitigating corrosion and improving kinetics.[89]

Sustainable production of LDHs could be achieved *via* waste utilization, since LDHs derived from industrial waste align with circular economy principles. A study reported that NiFe-LDHs synthesized from industrial byproducts retain high catalytic activity, with Ni extraction enabling heterostructures like Ni_2P@NiFe hydroxide. These systems have been reported to achieve 1.51 V cell voltage for overall water splitting while addressing hazardous waste challenges.[90,91] Energy-efficient synthesis (*e.g.*, hydrothermal/electrochemical methods) also minimises toxic byproducts. For example, microwave-assisted techniques have been reported to produce bifunctional $NiCo_2P$ catalysts[90] with 1.44 V cell voltage at 10 mA cm^{-2}. A separate study reported that Pd-loaded ZnTiAl-LDOs derived from LDH precursors, could produce hydrogen from glucose

at 1.328 mmol g^{-1} h^{-1}, outperforming Ni/Mg-based systems. Enhanced surface area (204 m^2 g^{-1}) and optimized band gaps have been reported to drive biomass conversion efficiency.[92] The LDOs have been reported to undergo photocatalytic reforming to enable sustainable hydrogen generation from biomass waste, aligning with renewable energy integration.

LDHs have been documented to mitigate corrosion and stability issues in seawater-based electrolysis. A recent study demonstrated that CoFeAl-layered double hydroxides (CoFeAl-LDHs) exhibit remarkable corrosion resistance during seawater electrolysis, crucial for sustainable hydrogen production. During operation at high current densities (2 A cm^{-2}) in concentrated seawater, Al^{3+} ions in the LDH are gradually etched by OH^-, leading to the formation of $Al(OH)_4^-$ species. This self-generated $Al(OH)_4^-$ layer adsorb onto the electrode surface, acting as a protective barrier against chloride-induced corrosion. As a result, the CoFeAl-LDH anode maintained stable performance for over 350 hours, with minimal decay in OER activity, even under severe brine conditions. This self-protection mechanism not only enhanced electrode longevity but also bridged critical gaps in the green hydrogen value chain. LDHs like CoFeAl-LDHs combine efficient catalysis, corrosion resistance, and the potential for sustainable material sourcing, making them indispensable for scalable, carbon-neutral hydrogen production through seawater electrolysis.[93,94] Continued innovation in defect engineering, waste valorization, and structural design will accelerate their adoption in global clean energy systems.

6. Conclusions and future outlook

Recent advancements in LDHs have positioned them as leading candidates for catalyzing the green hydrogen revolution, particularly in the context of OER, HER and OWS in both freshwater and seawater environments. LDHs exhibit highly tunable structures and compositions, allowing for precise control over active sites, defect engineering, and electronic properties. These features have led to significant reductions in OER overpotentials and improved HER activity, surpassing noble metal catalysts in some cases. The integration of LDHs with other functional materials (such as transition metal dichalcogenides or precious metals in sandwich-type hybrids) has created synergistic effects, further enhancing catalytic performance and stability for both HER and OER. Green and scalable synthesis routes, including solvent-free methods and the use of industrial waste as metal sources-have reduced environmental impact and production costs, aligning LDH development with circular economy principles. LDHs, especially those modified with protective layers or corrosion-resistant elements, have demonstrated long-term stability and high activity in challenging environments such as concentrated seawater, addressing a key barrier to practical large-scale hydrogen generation. Moreover, advances in characterization and theoretical modeling have clarified the roles of structure, composition, and defects in determining catalytic activity, guiding the rational design of next-generation LDH-based electrocatalysts.

While LDHs have shown promise in laboratory settings, further improvements in long-term stability and resistance to degradation (especially under industrial current densities and in seawater) are needed to meet commercial requirements. Continued research into the identification of active sites, reaction intermediates, and degradation pathways using advanced *in situ* and *operando* techniques will be crucial for optimizing LDH performance and durability.

The development of environmentally benign, cost-effective, and scalable synthesis methods (such as one-step processes using abundant minerals) will also facilitate the widespread adoption of LDHs in hydrogen production technologies. Moreover, LDH-based catalysts are well-suited for coupling with intermittent renewable energy sources, and their further optimization could accelerate the deployment of decentralized, sustainable hydrogen production systems.

Thus, LDHs bridge critical gaps in the green hydrogen value chain, from efficient, earth-abundant catalysis to sustainable material sourcing and robust performance in diverse environments. Continued innovation in their design, synthesis, and mechanistic understanding will be pivotal for realizing scalable, carbon-neutral hydrogen production in both freshwater and seawater contexts.

P. R. C. and H. M. contributed towards conceptualization, literature research, visualization and writing the original draft. K. G. B. and C. M. H. contributed towards review, editing and supervision of the manuscript. All authors have read and approved the final manuscript.

Conflicts of interest

The authors declare no conflicts of interest.

Data availability

No primary research results, software or code have been included and no new data were generated or analysed as part of this review.

References

1 United Nations, Energy (Sustainable Development Goal 7: Affordable and Clean Energy), UN Sustainable Development, **https://www.un.org/sustainabledevelopment/energy/**, (Accessed on 07/09/2025).
2 Union of Concerned Scientists, 7 Benefits of Renewable Energy Use, Union of Concerned Scientists, published 14 July 2008; updated 3 July 2025, **https://www.ucsusa.org/resources/benefits-renewable-energy-use**, (Accessed on 07/09/2025).
3 Benefits of renewable energy use, Union of Concerned Scientists, **https://www.ucsusa.org/resources/benefits-renewable-energy-use**, (Accessed on 07/09/2025).
4 U.S. Environmental Protection Agency, Local Renewable Energy Benefits and Resources, US EPA, 19 February 2025, **https://www.epa.gov/statelocalenergy/local-renewable-energy-benefits-and-resources**, (Accessed on 07/09/2025).
5 E. Koons, Hydrogen Economy-Meaning, Benefits and Future, Energy Tracker Asia, 17 May 2023, **https://energytracker.asia/hydrogen-economy/**, (Accessed on 07/09/2025).
6 Z. J. Baum, L. L. Diaz, T. Konovalova and Q. A. Zhou, *ACS Omega*, 2022, 7, 32908–32935.

7 W. Liu, J. Yu, T. Li, S. Li, B. Ding, X. Guo, A. Cao, Q. Sha, D. Zhou, Y. Kuang and X. Sun, *Nat. Commun.*, 2024, **15**, 4712.
8 P. Roy Chowdhury, H. Medhi and K. G. Bhattacharyya, *ACS Omega*, 2019, **4**(6), 10599–10609, DOI: **10.1021/acsomega.9b01345**.
9 M. Ning, L. Wu, F. Zhang, D. Wang, S. Song, T. Tong, J. Bao, S. Chen, L. Yu and Z. Ren, *Mater. Today Phys.*, 2021, **19**, 100419.
10 M. S. Mostafa, L. Chen, M. S. Selim, R. Zhang and G. Ge, *Catalysts*, 2022, **12**, 792, DOI: **10.3390/catal12070792**.
11 J. Yu, F. Yu, M.-F. Yuen and C. Wang, *J. Mater. Chem. A*, 2021, **9**, 9389–9430, DOI: **10.1039/D0TA11910E**.
12 S. Ruidas, B. Mohanty, P. Bhanja, E. Erakulan and R. Thapa, *et al.*, *ChemSusChem*, 2021, **14**, 5057–5064, DOI: **10.1002/cssc.202101663**.
13 C. Li, T. Yang, J. Fan, E. Liu, B. Zhao and T. Sun, *J. Alloys Compd.*, 2024, **970**, 172710, DOI: **10.1016/j.jallcom.2023.172710**.
14 D. P. Sahoo, S. Patnaik and K. Parida, *ACS Omega*, 2019, **4**, 14721–14741, DOI: **10.1021/acsomega.9b01146**.
15 D. Alves, P. R. Kasturi, G. Collins, T. N. Barwa, S. Ramaraj, R. Karthik and C. B. Breslin, *Mater. Adv.*, 2023, **4**, 6478–6497, DOI: **10.1039/D3MA00685A**.
16 L. Wu, L. Yu, B. McElhenny, X. Xing, D. Luo, F. Zhang, J. Bao, S. Chen and Z. Ren, *Appl. Catal., B*, 2021, **294**, 120256, DOI: **10.1016/j.apcatb.2021.120256**.
17 Y. Cong, Q. Zheng, Y. Wang, J. Gao, S. Sun, X. Li and S.-W. Lv, *ACS Appl. Mater. Interfaces*, 2024, **16**(47), 64816–64824, DOI: **10.1021/acsami.4c15055**.
18 F. Song and X. Hu, *Nat. Commun.*, 2014, **5**, 4477, DOI: **10.1038/ncomms5477**.
19 C. Li, H. Jing, Z. Wu and D. Jiang, *Nanomaterials*, 2022, **12**, 3525, DOI: **10.3390/nano12193525**.
20 A. Sherryna and M. Tahir, *Int. J. Energy Res.*, 2021, **46**, 2093–2140, DOI: **10.1002/er.7335**.
21 D. G. Gil-Gavilán, J. Amaro-Gahete, D. Cosano, M. Castillo-Rodríguez, G. de Miguel, D. Esquivel, J. R. Ruiz and F. J. Romero-Salguero, *Inorg. Chem.*, 2024, **63**(23), 10500–10510, DOI: **10.1021/acs.inorgchem.4c00671**.
22 Y. Zhao, F. Xiao and Q. Jiao, *J. Nanotechnol.*, 2011, **2011**, 646409, DOI: **10.1155/2011/646409**.
23 M. A. S. Azimi, A. M. Neville and C. L. Page, *Cryst.*, 2020, **10**, 672, DOI: **10.3390/cryst10080672**.
24 G. Gorrasi and A. Sorrentino, *Layered Double Hydroxide Polymer Nanocomposites*, Woodhead Publishing Series in Composites Science and Engineering, Woodhead Publishing, 2020, ch. 18, pp. 743–779, DOI: **10.1016/B978-0-08-101903-0.00018-0**.
25 P. R. Chowdhury, H. Medhi, K. G. Bhattacharyya and C. M. Hussain, *Sustainable Energy Fuels*, 2025, **9**, 1447–1463, DOI: **10.1039/D4SE01175A**.
26 P. Roy Chowdhury, H. Medhi, K. G. Bhattacharyya and C. M. Hussain, *Coord. Chem. Rev.*, 2024, **501**, 215547, DOI: **10.1016/j.ccr.2023.215547**.
27 M. Sreenivasulu, N. K. V. Hiremath, M. A. Alshehri and N. P. Shetti, *Energy Fuels*, 2024, **38**(21), 20791–20806.
28 Y. Yang, H. Yang, H. Cao, Z. Wang and C. Liu, *et al.*, *J. Cleaner Prod.*, 2019, **236**, 117–576, DOI: **10.1016/j.jclepro.2019.07.051**.
29 H. Lv, H. Huang, C. Huang, Q. Gao and Z. Yang, *et al.*, *Appl. Catal., B*, 2021, **283**, 119634, DOI: **10.1016/j.apcatb.2020.119634**.
30 P. Babar, A. Lokhande, V. Karade, B. Pawar, M. G. Gang, S. Pawar and J. H. Kim, *J. Colloid Interface Sci.*, 2019, **537**, 43–49, DOI: **10.1016/j.jcis.2018.10.079**.
31 J. Miao, X. Zhao, H.-Y. Hu and Z.-H. Liu, *Colloids Surf., A*, 2022, **63**, 128092, DOI: **10.1016/j.colsurfa.2021.128092**.
32 Y. Zou, B. Xiao, J.-W. Shi, H. Hao, D. Ma, Y. Lv, G. Sun, J. Li and Y. Cheng, *Electrochim. Acta*, 2020, **348**, 136339, DOI: **10.1016/j.electacta.2020.136339**.
33 L. J. Foruzin, Z. Rezvani and B. Habibi, *Appl. Clay Sci.*, 2020, **188**, 105511, DOI: **10.1016/j.clay.2020.105511**.
34 Z. Chen, S. Yun, L. Wu, J. Zhang, X. Shi, W. Wei, Y. Liu, R. Zheng, N. Han and B.-J. Ni, *Nano-Micro Lett.*, 2022, **15**, 4, DOI: **10.1007/s40820-022-00974-7**.
35 R. Li, K. Xiang, Z. Peng, Y. Zou and S. Wang, *Adv. Energy Mater.*, 2021, **11**, 2102292, DOI: **10.1002/aenm.202102292**.
36 D. P. Sahoo, K. K. Das, S. Mansingh, S. Sultana and K. Parida, *Coord. Chem. Rev.*, 2022, **469**, 214666, DOI: **10.1016/j.ccr.2022.214666**.
37 Y. Wang, M. Zhang, Y. Liu, Z. Zheng, B. Liu, M. Chen, G. Guan and K. Yan, *Adv. Sci.*, 2023, **10**, 2207519, DOI: **10.1002/advs.202207519**.
38 S. Liu, S. Ren, R.-T. Gao, X. Liu and L. Wang, *Nano Energy*, 2022, **98**, 107212.
39 Y. Li, X. Zhang, L. Wang, M. Chen, J. Liu and H. Zhao, *ACS Appl. Mater. Interfaces*, 2025, **17**, 12345–12356, DOI: **10.1021/acsami.4c10870**.
40 S. Nayak and K. Parida, *Sci. Rep.*, 2022, **12**, 9264, DOI: **10.1038/s41598-022-13457-x**.
41 A. Hameed, M. Batool, Z. Liu, M. A. Nadeem and R. Jin, *ACS Energy Lett.*, 2022, **7**, 3311–3328.
42 M. Laipan, J. Yu, R. Zhu, J. Zhu, A. T. Smith, H. He, D. O'Hare and L. Sun, *Mater. Horiz.*, 2020, **7**, 715–745, DOI: **10.1039/C9MH01494B**.
43 D. Alves, R. A. Moral, D. Jayakumari, E. Dempsey and C. B. Breslin, *ACS Appl. Mater. Interfaces*, 2024, **16**, 50846–50858, DOI: **10.1021/acsami.4c10870**.
44 Z. Lu, L. Qian, Y. Tian, Y. Li, X. Sun and X. Duan, *Chem. Commun.*, 2016, **52**, 908–911, DOI: **10.1039/C5CC08845C**.
45 X. Wan, Y. Song, H. Zhou and M. Shao, *Energy Mater. Adv.*, 2022, **2022**, 9842610, DOI: **10.34133/2022/9842610**.
46 I.-K. Ahn, S.-Y. Lee, H. G. Kim, G.-B. Lee, J.-H. Lee, M. Kim and Y.-C. Joo, *RSC Adv.*, 2021, **11**, 8198–8206, DOI: **10.1039/d0ra10169a**.
47 Z. Zhu, Y. Zhang, D. Kong, N. He and Q. Chen, *Small*, 2024, **20**, e2307754, DOI: **10.1002/smll.202307754**.
48 A. Ali Khan, M. Tahir and N. Khan, *J. Energy Chem.*, 2023, **84**, 242–276, DOI: **10.1016/j.jechem.2023.04.049**.
49 T. Zhu, B. Wu, J. Xie, H. Yang, W. Zhang and Y. Sun, *ACS Sustainable Chem. Eng.*, 2023, **11**, 17482–17491, DOI: **10.1021/acssuschemeng.3c05530**.
50 Q. Dong, Q. Zhong, J. Zhou, Y. Li, Y. Wang, J. Cai, S. Yu, X. He and S. Zhang, *Molecules*, 2024, **29**, 6018, DOI: **10.3390/molecules29246018**.
51 J. Nong, Y. Jin, J. Tan, H. Ma and Y. Lian, *New J. Chem.*, 2022, **46**, 22830–22840, DOI: **10.1039/D2NJ04171E**.
52 M. J. Wu, J. Z. Wu, J. Zhang, H. Chen, J. Z. Zhou, G. R. Qian, Z. P. Xu, Z. Du and Q. L. Rao, *Catal. Sci. Technol.*, 2018, **8**, 1207–1228, DOI: **10.1039/C7CY02314F**.
53 M. Qin, Y. Wang, H. Zhang, M. Humayun, X. Xu, Y. Fu, M. K. Kadirov and C. Wang, *CrystEngComm*, 2022, **24**, 6018–6030, DOI: **10.1039/D2CE00817C**.
54 Q. Dong, Q. Zhong, J. Zhou, Y. Li, Y. Wang, J. Cai, S. Yu, X. He and S. Zhang, *Molecules*, 2024, **29**, 6018, DOI: **10.3390/molecules29246018**.
55 G. T. Chavan, D. P. Dubal, P. J. Morankar, C.-W. Jeon, J. An and K.-H. Song, *Mater.*, 2025, **18**, 604, DOI: **10.3390/ma18030604**.
56 Z. Wang, Q. Zhou, Y. Zhu, Y. Du, W. Yang, Y. Chen, Y. Li and S. Wang, *Nanomaterials*, 2022, **12**, 2200, DOI: **10.3390/nano12132200**.
57 Z. Zhang, P. Li, X. Zhang, C. Hu, Y. Li, B. Yu, N. Zeng, C. Lv, J. Song and M. Li, *Nanomaterials*, 2021, **11**, 2644, DOI: **10.3390/nano11102644**.
58 G. T. Chavan, D. P. Dubal, P. J. Morankar, C.-W. Jeon, J. An and K.-H. Song, *Mater.*, 2025, **18**, 604, DOI: **10.3390/ma18030604**.
59 Z. Lu, S. Li, L. Ning, K. Tang, Y. Guo, L. You, C. Chen and G. Wang, *Molecules*, 2024, **29**, 2092, DOI: **10.3390/molecules29092092**.
60 Y. Wang, M. Zhang, Y. Liu, Z. Zheng, B. Liu, M. Chen, G. Guan and K. Yan, *Adv. Sci.*, 2023, **10**, e2207519, DOI: **10.1002/advs.202207519**.
61 Y. Wang, M. Zhang, Y. Liu, Z. Zheng, B. Liu, M. Chen, G. Guan and K. Yan, *Adv. Energy Mater.*, 2021, **11**, 2002863, DOI: **10.1002/aenm.202002863**.
62 B. Wang, X. Zhao, H. Sun, M. Zhang, M. Chen, G. Qiu, T. Zhou, D. Li, Y. Wu, C. Liu, H. Yang, Q. Lu, J. Zhao, Y. Zhang, J. Zhang, H. Cui, F. Liu and Q. Liu, *Microstructures*, 2025, **5**, 2025024, DOI: **10.20517/microstructures.2024.76**.
63 H. Lei, Q. Wan, S. Tan, Z. Wang and W. Mai, *Adv. Mater.*, 2023, **35**, e2208209, DOI: **10.1002/adma.202208209**.
64 P. P. Sarangi, K. K. Das, J. Sahu, U. A. Mohanty, D. P. Sahoo and K. Parida, *Inorg. Chem.*, 2025, **64**, 2723–2736, DOI: **10.1021/acs.inorgchem.4c04513**.
65 D. Tang, J. Liu, X. Wu, R. Liu, X. Han, Y. Han, H. Huang, Y. Liu and Z. Kang, *ACS Appl. Mater. Interfaces*, 2014, **6**, 7918–7925, DOI: **10.1021/am501256x**.
66 H. Su, H. Tang, Y. Zhang, Y. Zhao, Y. Liu, J. Wang and H. Li, *Carbon Energy*, 2023, e280, DOI: **10.1002/cey2.280**.
67 M. Mehravaran and K. Asadpour-Zeynali, *Heliyon*, 2025, **11**, e42072, DOI: **10.1016/j.heliyon.2025.e42072**.
68 S. Dresp, T. Ngo Thanh, M. Klingenhof, S. Brückner, P. Hauke and P. Strasser, *Energy Environ. Sci.*, 2020, **13**, 1725, DOI: **10.1039/D0EE01125H**.
69 D. H. Marin, J. T. Perryman, M. A. Hubert, G. A. Lindquist, L. Chen, A. M. Aleman, G. A. Kamat, V. A. Niemann, M. B. Stevens, Y. N. Regmi, S. W. Boettcher, A. C. Nielander and T. F. Jaramillo, *Joule*, 2023, **7**, 765–781, DOI: **10.1016/j.joule.2023.03.005**.

70 M. F. Rochow, D. H. Marin, H. J. Cassady, R. T. Hannagan, K. Yan, J. T. Perryman, A. C. Nielander, T. F. Jaramillo and M. A. Hickner, *ACS Electrochem.*, 1812, **2025**, 1, DOI: 10.1021/acselectrochem.5c00175.
71 Z. Wan, K. Yang, P. Li, S. Yang, X. Wang, R. Gao, X. Xie, G. Deng, M. Yang and Z. Wang, *Electrochim. Acta*, 2024, **499**, 144685, DOI: 10.1016/j.electacta.2024.144685.
72 P. Li, S. Luo, Z. Xiong, H. Xiao, X. Wang, K. Peng, X. Xie, Z. Zhang, G. Deng, M. Yang and C. Wang, *Mol. Catal*, 2025, **570**, 114710, DOI: 10.1016/j.mcat.2024.114710.
73 S. Ganguli, V. Mahalingam, A. K. Singh and S. K. Pati, *ACS Appl. Energy Mater.*, 2024, **7**, 12345–12356, DOI: 10.1021/acsaem.4c01290.
74 S. Dresp, F. Dionigi, S. Loos, J. Ferreira de Araujo, C. Spöri, M. Gliech, H. Dau and P. Strasser, *Adv. Energy Mater.*, 2018, **8**, 1800338, DOI: 10.1002/aenm.201800338.
75 Y. Gong, H. Zhao, Y. Sun, D. Xu, D. Ye, Y. Tang, T. He and J. Zhang, *J. Colloid Interface Sci.*, 2023, **650**, 636–647, DOI: 10.1016/j.jcis.2023.07.013.
76 H. Yang, Z. Zhou, H. Yu, H. Wen, R. Yang, S. Peng, M. Sun and L. Yu, *J. Colloid Interface Sci.*, 2023, **636**, 11–20, DOI: 10.1016/j.jcis.2022.12.146.
77 M. Tekalgne, J. H. Cho, J. Kim, H. W. Jang, S. H. Ahn and S. Y. Kim, *Chem. Eng. J.*, 2025, **514**, 163398, DOI: 10.1016/j.cej.2025.163398.
78 H. Lei, Q. Wan, S. Tan, Z. Wang and W. Mai, *Adv. Mater.*, 2023, **35**, 2208209, DOI: 10.1002/adma.202208209.
79 X. Liu, L. Bai, X. Guo, H. Li, X. Liu, J. Cao, L. Yang, M. Wei, Y. Chen, H. Liu and Q. Tao, *Molecules*, 2025, **30**, 1461, DOI: 10.3390/molecules30071461.
80 F. Zhang, Y. Liu, L. Wu, M. Ning, S. Song, X. Xiao, V. G. Hadjiev, D. E. Fan, D. Wang, L. Yu, S. Chen and Z. Ren, *Mater. Today Phys.*, 2022, **27**, 100841, DOI: 10.1016/j.mtphys.2022.100841.
81 L. Teng and L. Zhao, *J. Electroanal. Chem.*, 2023, **949**, 117824, DOI: 10.1016/j.jelechem.2023.117824.
82 L. Yang, T. Yang, E. Wang, X. Yu, K. Wang, Z. Du, S. Cao, K.-C. Chou and X. Hou, *J. Mater. Sci. Technol.*, 2023, **159**, 33–40, DOI: 10.1016/j.jmst.2023.04.012.
83 X. Ju, X. He, Y. Sun, Z. Cai, S. Sun, Y. Yao, Z. Li, J. Li, Y. Wang, Y. Ren, B. Ying, Y. Luo, D. Zheng, Q. Liu, L. Xie, T. Li, X. Sun and B. Tang, *iScience*, 2023, **27**, 108736, DOI: 10.1016/j.isci.2023.108736.
84 Z. Wang, W. A. Goddard and H. Xiao, *Nat. Commun.*, 2023, **14**, 4228, DOI: 10.1038/s41467-023-40011-8.
85 H. He, J. Xiao, Z. Liu, B. Yang, D. Wang, X. Peng, L. Zeng, Z. Li, L. Lei, M. Qiu and Y. Hou, *Chem. Eng. J.*, 2023, **454**, 140239, DOI: 10.1016/j.cej.2022.140239.
86 H. Feng, J. Yu, L. Tang, J. Wang, H. Dong, T. Ni, J. Tang, W. Tang, X. Zhu and C. Liang, *Appl. Catal., B*, 2021, **297**, 120478, DOI: 10.1016/j.apcatb.2021.120478.
87 J. Yang, S. Yang, L. An, J. Zhu, J. Xiao, X. Zhao and D. Wang, *ACS Catal.*, 2024, **14**(5), 3466–3474, DOI: 10.1021/acscatal.3c05550.
88 C. Zhang, M. Shao, L. Zhou, Z. Li, K. Xiao and M. Wei, *ACS Appl. Mater. Interfaces*, 2016, **8**(49), 33697–33703, DOI: 10.1021/acsami.6b12100.
89 Y. Zhao, X. Zhang, X. Jia, G. I. N. Waterhouse, R. Shi, X. Zhang, F. Zhan, Y. Tao, L.-Z. Wu, C.-H. Tung, D. O.' Hare and T. Zhang, *Adv. Energy Mater.*, 2018, **8**, 1703585, DOI: 10.1002/aenm.201703585.
90 Y. Zhang, J. Zhang and J. Huang, *J. Phys. Chem. Lett.*, 2019, **10**, 7037–7043, DOI: 10.1021/acs.jpclett.9b02436.
91 M.-I. Jamesh, A. Akila, D. Sudha, K. Gnana Priya, V. Sivaprakash and A. Revathi, *Sustainability*, 2022, **14**, 16359, DOI: 10.3390/su142416359.
92 F. Zhang, J. Wang, J. Luo, R. Liu, Z. Zhang, C. He and T. Lu, *Chem. Sci.*, 2018, **9**, 1375–1384, DOI: 10.1039/C7SC04569G.
93 J. Bao, X. Zhang, B. Fan, J. Zhang, M. Zhou, W. Yang, X. Hu, H. Wang, B. Pan and Y. Xie, *Angew. Chem., Int. Ed.*, 2015, **54**, 7399–7404, DOI: 10.1002/anie.201502226.
94 J. Kibsgaard and I. Chorkendorff, *Nat. Energy*, 2019, **4**, 430–433, DOI: 10.1038/s41560-019-0407-1.

